UC Berkeley
UC Berkeley Previously Published Works

Title

The endoplasmic reticulum P5A-ATPase is a transmembrane helix dislocase

Permalink

Journal

ISSN

Authors

McKenna, Michael J
Sim, Sue Im
Ordureau, Alban
et al.

Publication Date

DOI

Peer reviewed

The endoplasmic reticulum P5A-ATPase is a transmembrane helix dislocase

Michael J. McKenna[#1], **Sue Im Sim**[#2], **Alban Ordureau**[1], **Lianjie Wei**[1,‡], **J. Wade Harper**[1], **Sichen Shao**[1,*], **Eunyong Park**[2,3,*]

[1]Department of Cell Biology, Harvard Medical School, Blavatnik Institute, Boston, MA 02115, USA.

[2]Department of Molecular and Cell Biology, University of California, Berkeley, CA 94720, USA.

[3]California Institute for Quantitative Biosciences, University of California, Berkeley, CA 94720, USA.

[#] These authors contributed equally to this work.

Abstract

Organelle identity depends on protein composition. How mistargeted proteins are selectively recognized and removed from organelles is incompletely understood. Here we found that the orphan P5A-ATPase transporter ATP13A1 (Spf1 in yeast) directly interacted with the transmembrane segment (TM) of mitochondrial tail-anchored proteins. P5A-ATPase activity mediated the extraction of mistargeted proteins from the endoplasmic reticulum (ER). Cryo-EM structures of *Saccharomyces cerevisiae* Spf1 revealed a large membrane-accessible substrate-binding pocket that alternately faced the ER lumen and cytosol, and an endogenous substrate resembling an α-helical TM. Our results indicate that the P5A-ATPase could dislocate misinserted hydrophobic helices flanked by short basic segments from the ER. TM dislocation by the P5A-ATPase establishes an additional class of P-type ATPase substrates and may correct mistakes in protein targeting or topogenesis.

One Sentence Summary:

Cryo-EM structures and functional analyses reveal that the orphan P5A-ATPase dislocates misinserted transmembrane helices from the endoplasmic reticulum.

---

[*]Corresponding author. sichen_shao@hms.harvard.edu (S.S.); eunyong_park@berkeley.edu (E.P.).
[‡]Current address: Biochemistry, Biophysics, and Structural Biology Program, Division of Biology and Biomedical Sciences, Washington University in St. Louis, St. Louis, MO 63110, USA.

Over one third of the proteome in eukaryotes consists of membrane and secretory proteins with diverse hydrophobic sequences that must insert correctly into the appropriate cellular membrane. Protein mistargeting causes organelle dysfunction and cellular and organismal stress (1, 2), underscoring the importance of quality control (QC) mechanisms that remove mislocalized proteins. Defined by a single C-terminal transmembrane segment (abbreviated TM), tail-anchored (TA) proteins pose a distinct sorting challenge because they rely exclusively on posttranslational mechanisms to localize to the endoplasmic reticulum (ER), mitochondria, or peroxisomes. While TA protein targeting to the ER is well-studied (3), how cells remove mistargeted TA proteins from the ER and properly localize non-ER TA proteins is poorly understood.

A yeast genetic screen for mutants that disrupt mitochondrial TA protein localization identified only *SPF1*, whose deletion results in mitochondrial TA protein accumulation at the ER (4). *SPF1* encodes the ER-resident orphan P5A-ATPase, a conserved subtype of the eukaryotic-specific P5 subfamily of P-type ATPases. P-type ATPases are a major class of active transporters found in all organisms that pump substrates across membranes through conformational changes driven by phosphorylation and dephosphorylation of a conserved aspartate (5-7). Among the five subfamilies categorized by sequence similarity, the functions of P1- to P3-ATPases as cation transporters and P4-ATPases as lipid flippases are well-defined. In addition, ATP13A2, one of four mammalian P5B-ATPases, was recently proposed to be a lysosomal polyamine transporter (8). Otherwise, little is known about the substrates and biological functions of P5-ATPases.

Humans and yeast each have a single P5A-ATPase, ATP13A1 and Spf1, respectively, which likely perform a conserved task based on functional complementations (9, 10). In addition to disrupting TA protein localization and turnover (4, 11), mutating *SPF1* causes a wide spectrum of phenotypes, including induction of the ER unfolded protein response (UPR), defects in lipid and sterol homeostasis, and dysregulated protein N-glycosylation, topogenesis, and turnover (10, 12-20). It has been speculated that these pleiotropic phenotypes may be explained by the P5A-ATPase functioning as a manganese or calcium transporter, or as a lipid flippase (13-15, 18, 21). However, direct evidence supporting any of these functions is lacking, and the identity of physiological P5A-ATPase substrates remains elusive. Here, using cell-free reconstitutions, high-resolution cryo-EM, and proteomics, we found that the P5A-ATPase could dislocate moderately hydrophobic terminal transmembrane helices from the ER membrane, a mechanism required to ensure correct mitochondrial TA protein localization.

P5A-ATPases directly interact with TMs

We used an unbiased strategy to identify factors that directly interacted with a model TA protein containing the mitochondrial OMP25 TM during reconstituted targeting reactions (Fig. 1A). We incorporated the UV-activated crosslinker p-benzoyl-L-phenylalanine (Bpa) into the TM [referred to as TA(Bpa)] and purified recombinant, FLAG-tagged TA(Bpa) in complex with calmodulin (CaM), a calcium-dependent TM chaperone (fig. S1A) (22, 23). We confirmed that FLAG-TA(Bpa) released from CaM by EGTA formed UV-dependent crosslinks to the TM chaperone SGTA (24) (Fig. 1B and fig. S1C). When we released

FLAG-TA(Bpa) in the presence of crude yeast membranes that could reconstitute TM insertion (fig. S1B), we observed crosslinks to various proteins. Because photocrosslinking generates covalent adducts, we expected this approach to enrich for otherwise transient interactions made by substrates undergoing targeting or QC. Indeed, tandem mass tag mass spectrometry (TMT-MS) analysis of UV-dependent membrane interactors of FLAG-TA(Bpa) identified known mitochondrial protein receptors and QC factors (Fig. 1C, fig. S1D, and Data S1) (25-27). Unexpectedly, the ER-resident P5A-ATPase Spf1 was a prominent UV-dependent interactor of FLAG-TA(Bpa) (Fig. 1C,D).

Although Spf1 has been linked to mitochondrial TA protein mislocalization (4, 11), a direct interaction has not been reported. To confirm the interaction between P5A-ATPases and TA proteins, we translated radiolabeled TA(Bpa) in vitro and performed site-specific crosslinking with crude yeast membranes or human ER-derived rough microsomes (RMs) containing FLAG-tagged Spf1 or ATP13A1, respectively. UV-dependent TA protein crosslinks to each P5A-ATPase were detected after denaturing immunoprecipitations (Fig. 1E and fig. S2). Crosslinking was specific to Bpa positioned within the TM but not the cytosolic domain and enhanced by flanking C-terminal sequences that contain basic residues (Fig. 1E), a common feature of mitochondrial TA proteins. Thus, the P5A-ATPase directly interacts with TMs.

ATP13A1 mediates ATP-dependent TM dislocation

To investigate if P5A-ATPase activity affected TA protein localization to the ER, we performed in vitro insertion reactions of radiolabeled TA protein with RMs isolated from wildtype (WT) or ATP13A1 knockout (KO) cells without or with re-expression of ATP13A1 (fig. S3A). TA protein containing the OMP25 TM preferentially accumulated in RMs lacking WT ATP13A1 activity (fig. S3B-D). Two possibilities may explain this result: deleting ATP13A1 may enhance TM insertion (4), or impair TM extraction. To distinguish between these scenarios, we uncoupled OMP25 TM insertion and extraction by re-isolating RMs after short insertion reactions for extraction assays with an energy regenerating system and excess SGTA to sequester dislocated TMs (Fig. 2A) (28). WT RMs displayed significantly higher extraction activity than KO RMs based on the amount of TA protein dislocated into the soluble fraction and bound to SGTA (Fig. 2B,C and fig. S4A). TM removal required ATP (fig. S4B), and the impaired dislocation activity of KO RMs was rescued by WT but not D533A ATP13A1, a catalytically inactive variant in which the conserved phosphorylation site required for transport is mutated. Thus, ATP13A1 mediates ATP-dependent removal of a mitochondrial TM from the ER.

ATP13A1 minimizes TA protein mislocalization

We next examined how ATP13A1 affects TA protein localization in human cells. In WT cells, FLAG-tagged mitochondrial TA protein reporters containing either the OMP25 or BAK1 TM (referred to as OMP25 or BAK1) localized to mitochondria as expected (Fig. 2D,E and fig. S5A,B). Knocking out ATP13A1 resulted in substrate-specific changes in TA protein levels, in which OMP25 levels decreased and BAK1 levels increased (fig. S5C,D). Both mitochondrial TA proteins displayed increased mislocalization to the ER and other

secretory pathway organelles in ATP13A1 KO cells (Fig. 2D, fig. S5 and S6), consistent with *spf1* yeast phenotypes (4, 11). Localization of TA proteins with ER-targeted TMs was not affected by ATP13A1 KO (fig. S6). Re-expressing WT, but not D533A, ATP13A1 in KO cells restored localization and expression levels of both OMP25 and BAK1 (Fig. 2D,E and fig. S5). Thus, ATP13A1 is required for proper mitochondrial TA protein localization.

To confirm that mitochondrial TA protein mislocalization in ATP13A1 KO cells was due to impaired TM removal from the ER rather than altered insertion efficiencies, we assayed the targeting of in vitro translated OMP25 to organelles of semi-permeabilized cells over short time periods to minimize downstream processes (fig. S7A). OMP25 localized similarly to mitochondria in both WT and KO semi-permeabilized cells (fig. S7B,C), indicating that ATP13A1 was not required for initial TA protein targeting. Nonetheless, at steady state, mitochondrial TA proteins were not only mislocalized, but also apparently depleted from mitochondria in ATP13A1 KO cells (Fig. 2D, fig. S5A and S7C). Because targeting to mitochondria was not affected, we reasoned that this observation may have resulted from other mechanisms. In particular, the AAA-ATPase Msp1 (ATAD1 in humans) can extract TMs from the outer mitochondrial membrane (26, 28, 29). Knocking down ATAD1 in ATP13A1 KO cells significantly restored mitochondrial localization of both BAK1 and OMP25 (fig. S8A-C). These results support a model in which ATAD1 and ATP13A1 each facilitates TM removal from mitochondria and the ER, respectively, to contribute to TA protein localization at steady state (fig. S8D). Impairing ATP13A1 would result in the ER acting as a "sink" that accumulates misinserted TMs owing to the disruption of a major mechanism for removing them. In the absence of ATP13A1, misinserted TA proteins appear to undergo alternative substrate-specific processes that may include vesicular trafficking and lysosomal or ER-associated degradation (11, 30).

Features of ATP13A1-dependent proteins

The observation that re-expressing WT ATP13A1 in KO cells restored mitochondrial TA protein reporter levels suggested that some endogenous proteins that require ATP13A1 function could be identified by quantitative proteomics. Towards this end, we analyzed lysates of WT, ATP13A1 KO, and rescue cells using TMT-MS (fig. S9A and Data S2). We identified 34 proteins with decreased abundance in ATP13A1 KO cells whose abundance was specifically rescued by acutely re-expressing WT but not D533A ATP13A1 (Fig. 2F, fig. S9B and S10A-D). Except for one, all of these candidates were mitochondria- or ER-targeted proteins.

Endogenous OMP25 and two additional mitochondrial TA proteins, MAVS and MAOB, were among these candidates, consistent with the decrease in OMP25 reporter levels in ATP13A1 KO cells that was rescued by WT ATP13A1 (fig. S4A). Another identified mitochondrial protein, RMDN3, has a single N-terminal TM which inserts in the N_{lumen}/C_{cyto} orientation. These candidates all have a TM flanked by a short positively charged lumenal segment (fig. S10A). Immunofluorescence verified mislocalization of endogenous OMP25 and RMDN3 in ATP13A1 KO cells which was specifically rescued by re-expressing WT ATP13A1 (Fig. 2G and fig. S10E, F).

The remaining ATP13A1-dependent proteins contain an N-terminal ER-targeting signal sequence or type II TM, which should adopt an N_{cyto}/C_{lumen} topology (fig. S10B) (31). Proteins without an N-terminal hydrophobic helix were not enriched, arguing against a general defect in ER protein maturation. Although highly diverse, signal sequences and type II TMs are generally less hydrophobic than TMs of the opposite topology and often have positively charged N-termini (32). The N-termini of candidate signal sequences also appear enriched in prolines (fig. S10B,G). These biophysical features resemble mitochondrial TA proteins and raise the possibility that ATP13A1 may mediate the removal of these terminal hydrophobic helices if they are inserted in the wrong orientation (N_{lumen}/C_{cyto}) (fig. S10B,H). Together, our data support a QC function for P5A-ATPases in removing misinserted terminal hydrophobic helices from the ER.

Cryo-EM structure of apo Spf1

The P5A-ATPase is an orphan transporter, and our results suggesting a role in TM dislocation were puzzling because P-type ATPases are generally assumed to transport cations or lipids. To understand the substrate selectivity of this family of transporters, we determined the structure of the P5A-ATPase Spf1 from *S. cerevisiae* using single-particle cryo-EM (Fig. 3A,B and table S1). We attached a green-fluorescent protein (GFP) tag to the 3' end of the chromosomal *SPF1* gene and extracted endogenous Spf1 from yeast membranes with a dodecyl maltoside (DDM)/cholesteryl hemisuccinate (CHS) mixture. Spf1 purified using anti-GFP nanobody affinity resin eluted as a single peak in size-exclusion chromatography (fig. S11A,B). Cryo-electron micrographs of apo Spf1, purified without any nucleotide or phosphate analogs, displayed well-dispersed particles (fig. S11C). Two-dimensional (2D) image classification was used to remove empty micelles and some poor quality particles (fig. S11D,E), resulting in 216,994 particles that showed 2D projections of Spf1 from various angles with clear protein features (fig. S11E). Ab-initio reconstruction and three-dimensional (3D) classification indicated that most Spf1 molecules were in a single conformation (fig. S11D). ~60% of particles from 2D classification were used to reconstruct the final apo map at 3.5-Å resolution (Fig. 3A, movie S1, and fig. S11D-G). Many sidechains were clearly visible, enabling de novo building of an atomic model (fig. S12).

The apo Spf1 structure showed all core domains of P-type ATPases, namely the cytosolic A (actuator), P (phosphorylation), and N (nucleotide binding) domains and the T (transport) domain formed by TMs 1–6 (Fig. 3A-C and fig. S13). In addition, as is common in P2- to P5-type ATPases, Spf1 contains an S (support) domain (TMs 7–10) that tightly packs against TM5 and TM6. The structure also showed two features unique to the P5A-ATPase: an N-terminal domain (NTD) preceding the A domain and an "arm"-like elongated domain protruding between the P domain and TM5. The NTD contains a seven-stranded β-barrel in the cytosol, which is tightly bound to the A domain, and two additional TMs (TMa and TMb), which appear to be only loosely associated with TMs 1 and 2 via lipid/detergent molecules (fig. S14A). The arm domain extends from the P domain with a conserved α-helix and positions its distal portion upon the detergent micelle (Fig. 3A and fig. S14B). An atomic model for this region could not be built owing to poor local resolution, but the

micelle around the contact was noticeably pulled up toward the arm domain (fig. S14B), suggesting that the arm domain might affect local membrane structure.

Apo Spf1 has a large inward-open substrate binding pocket

In all P-type ATPases, the substrate-binding site is formed mainly by TM2, TM4, and TM6 of the T-domain at the point where the TM4 helix is disrupted (in Spf1, at the PP[E/D]LP motif between TM4a and TM4b). Apo Spf1 also shows a prominent pocket for substrate binding in this site, but with an unusually large V-shaped cavity compared to other P-type ATPases (Fig 3D and fig. S15). The pocket is blocked on the ER luminal side and open toward the cytosol. Thus, the apo structure represents an inward-open conformation of the transporter. The inner surface is lined with a mixture of hydrophilic and hydrophobic side chains (fig. S15A,C) and exhibits negative electrostatic potential (fig. S16A) that is contributed collectively by D215, E232, D434, E446, and E450. These acidic amino acids are highly conserved in P5A-ATPases across species but not in the closest subfamily of P5B-ATPases (fig. S16B).

One striking feature of the putative substrate-binding pocket is that it is open both to the cytosol and laterally toward the lipid phase in the cytosolic leaflet of the ER membrane between TM2 and TM6 (Fig. 3D and fig. S15A). In P2-ATPase cation pumps, such as the sarcoplasmic/endoplasmic reticulum Ca^{2+}-ATPase (SERCA) and Na^+,K^+-ATPase, the T domain forms a small ion-binding cavity that is shielded away from the membrane (33-37). In P4-ATPase lipid flippases, the equivalent pocket, which is also small and binds to a phospholipid headgroup, is exposed only to the lipid phase (38-40). The unusual size and topology of the substrate pocket suggests that the P5A-ATPase has fundamentally different substrate specificities than other P-type ATPases with known structures. Notably, the structure did not reveal any sites in the pocket of Spf1 that could specifically coordinate a metal ion, arguing against the idea that the P5A-ATPase transports cations (10, 18).

Structure of Spf1 in an outward-open conformation

P-type ATPases undergo a series of conformational changes with ATP binding, phosphorylation of a conserved aspartate (D487 in Spf1, D533 in ATP13A1), and subsequent dephosphorylation in a scheme known as the Post-Albers cycle (i.e., E1 → E1-ATP → E1P-ADP → E1P → E2P → E2-Pi → E1; fig. S17A). Transitions between the E1 and E2 states result in large conformational changes in the T domain that mediate substrate transport. Because the apo structure of Spf1 represents only the E1 form, we sought to elucidate different conformational states by adding nucleotide or phosphate analogs to purified Spf1. To this end, we obtained structures of Spf1 in complex with AMP-PCP, AlF_4^-, and BeF_3^-, at overall resolutions of 3.7 Å, 3.4 Å, and 3.3 Å (fig. S18). AMP-PCP, a non-hydrolyzable ATP analog, locks the enzyme in an ATP-bound state, and the phosphate analogs AlF_4^- and BeF_3^- form a stable complex with the side-chain carboxylate of D487 to mimic a phosphorylated aspartate (37). All three structures show clear EM density for these inhibitors bound at the phosphorylation site (fig. S19A-C). Based on the arrangement of the A, P, and N domains and comparison with other P-type ATPase structures (37, 39), we assigned the AMP-PCP, AlF_4^-, and BeF_3^- structures as the E1-ATP, E1P, and E2P states,

respectively. The AMP-PCP- or AlF_4^- - bound Spf1 structures were essentially identical to the apo structure (RMSD of 0.56 Å and 0.48 Å; fig. S19D,E). Only a slight (7°) inward rotation was seen with the N domain of AMP-PCP-bound Spf1 as AMP-PCP bridges the interface of the N and P domains. Importantly, the T domain maintained the inward-open conformation in both the AMP-PCP- and AlF_4^--bound structures.

In contrast, the BeF_3^--bound E2P structure showed a drastically different conformation (Fig. 4A,B, movie S2, and fig. S19F,G). Similar to other P-type ATPases, the N domain of Spf1 undergoes a large (~50°) outward rotation with respect to the P domain during the E1P to E2P transition. This allows the A domain, which contains a conserved (S/T)GES motif for dephosphorylation, to access the phosphorylation site via a ~24° inward rotation of the A domain and NTD toward the N-P interface. As TM1 and TM2 are linked to the A domain, this motion dramatically restructures the substrate-binding pocket. TM2 and TM6, which contact each other on the ER luminal side in a V-shaped arrangement in the E1 states, spread out into a parallel arrangement, and the cytosolic segment of TM4 (denoted TM4b) moves in between TM2 and TM6 toward the lipid phase by a tilting motion (Fig. 4D and movie S3). Consequently, the inward-open V-shaped substrate pocket transforms into an outward-open, inverted "U"-shaped pocket (Fig. 4C,D, and fig. S15B). During this E1 to E2 transition, the lateral opening to the lipid phase is maintained but shifts from the cytosolic to the luminal leaflet of the ER membrane (movie S3). The surface of the pocket maintains a negative electrostatic potential (Fig. 4C), suggesting that substrates likely contain positive charges in addition to a hydrophobic component which would interact with the acyl chains of lipids at the lateral opening. These features are remarkably consistent with the TMs of mitochondrial TA proteins and the terminal hydrophobic helices of ATP13A1-dependent proteins identified in our proteomics analyses (Fig. 2F).

Visualization of a putative Spf1 substrate

Finally, we sought to visualize substrate-engaged Spf1. Although we did not observe substrate density in the structures obtained with Spf1 purified as described above, we reasoned that endogenous substrates may co-purify with Spf1 trapped in the outward-open E2P conformation. Accordingly, we repeated the extraction and purification of Spf1 with BeF_3^- included in all buffers. The resulting 3.3-Å-resolution structure (fig. S18J-L,P) was essentially identical to the E2P structure but with a prominent difference—an additional elongated density of a putative substrate traversing the lateral opening of the substrate pocket (Fig. 4E and fig. S20A).

The putative substrate density spans almost the entire membrane and closely resembles an α-helical TM that can accommodate a 20-residue-long polyalanine model (Fig. 4E,F). Notably, the large cylindrical shape is incompatible with detergents, lipids, and sterols (fig. S20B). In the cytosolic leaflet of the membrane, the density is exposed to the lipid phase and may interact with hydrophobic amino acids of TM2 (F223, M227, M231), TM4b (M449, M453), and the conserved PP(E/D)LP motif (P445) between TM4a and TM4b. In the luminal leaflet, the density is directed to the inverted U-shaped pocket. This density likely represents an average of multiple different co-purified substrates, possibly explaining the

lower resolution compared to Spf1. Altogether, our structural and functional data indicate that P5A-ATPases dislocate misinserted TMs from the ER membrane.

Discussion

Our results assign transmembrane helices as the substrates of the ER-resident P5A-ATPase, thereby defining an additional P-type ATPase function of transporting polypeptides out of lipid bilayers. Until recently, P-type ATPases were thought to be exclusively cation or lipid pumps. Together with the report that the P5B-ATPase ATP13A2 may transport polyamines (8), our study reveals that P-type ATPases mediate transport of surprisingly diverse substrates. While the T-domains of all P-type ATPases display a similar overall arrangement of TMs 1–6, our structures demonstrate that they can form fundamentally different substrate binding sites. The large substrate binding pocket of Spf1, whose opening not only alternately faces the cytosol and the ER lumen but also remains laterally accessible from the membrane, is unique among P-type ATPases characterized to date. We propose that the P5A-ATPase uses this unique pocket to extract mistargeted or misinserted TMs with a short flanking luminal hydrophilic segment from the ER (Fig. 5). In this working model, we hypothesize that the substrate TM largely remains in the lipid phase while the luminal segment is flipped across the membrane by the outward- to inward-open transition of the large cavity in the T domain. Moderate hydrophobicity characteristic of signal sequences and mitochondrial TMs may lower the energetic barrier for dislocation. Positive charges in the luminal segment may be preferred clients, while large luminal segments are likely excluded owing to the limited space in the pocket.

TM dislocation by the P5A-ATPase also reveals a previously unidentified protein QC and safeguarding mechanism at the ER. Active transport by the P5A ATPase is required to dislocate mitochondrial TMs that mistarget to the ER. P5A-ATPase function at the ER appears similar to Msp1 at the outer mitochondria membrane: although structurally unrelated, both use ATP as an energy source to dislocate TMs, possibly providing opportunities for re-insertion into the correct membrane. This idea is consistent with emerging observations that ER and mitochondrial factors cooperate to degrade aberrant TM-containing proteins (11, 30) and to ensure high-fidelity mitochondrial protein import, as in the 'ER-SURF' pathway (41). The P5A-ATPase may also dislocate ER-targeted N-terminal hydrophobic helices, such as signal sequences, that erroneously insert in the N_{lumen}/C_{cyto} orientation, although the exact basis of these substrates' dependence on P5A-ATPases remains unclear. Biophysical features of P5A-ATPase-dependent clients resemble substrates of the ER membrane protein complex (EMC), which inserts moderately hydrophobic TA proteins and terminal TMs in the N_{lumen}/C_{cyto} orientation (23, 42). EMC and the P5A-ATPase may thus have mechanistically opposing activities at the ER. Disruption of EMC also causes a wide-range of ER-related dysfunction (17, 43), similar to the pleiotropic phenotypes associated with P5A-ATPase mutants. Thus, cells appear to spread the burden of managing very diverse TMs by employing an arsenal of different machineries—each with varying substrate selectivity—that collaborate to fine tune TM localization and topology.

Materials and Methods

Plasmids and antibodies

To express recombinant TA protein in complex with CaM (fig. S1A), the open reading frame of a model TA protein containing the cytosolic domain of SEC61β and OMP25 TM as described in (44) was appended after a 3C protease cleavage site to the coding sequence of pGEX-CaM (22). N-terminal FLAG tags and amber codons were introduced using conventional molecular biology techniques. pGEX-SGTA (24), pEVOL-Bpa for expressing amber codon suppression components in bacteria (45), and plasmids for expressing recombinant Bpa-RS and for suppressor tRNA transcription (46) have been described.

SP64-based plasmids used to generate in vitro transcription templates were as previously described (47). TM substitutions and introduction of amber stop codons for Bpa incorporation (e.g. Fig. 1E) were accomplished using conventional Gibson assembly and Phusion mutagenesis approaches. Model TA protein coding sequences were transferred to pcDNA5/FRT/TO vectors for stable incorporation into Flp-In T-REx HeLa cells (gift from Brian Raught) behind a doxycycline-inducible CMV promoter (e.g. Fig. 2D,E). TM sequences were exchanged using Gibson assembly.

ATP13A1 cDNA (Harvard plasmID HsCD00082872) was cloned into pcDNA5/FRT/TO behind an N-terminal 3xFLAG tag by restriction enzyme digestion and Gibson assembly. Sequence encoding the N-terminal 132 amino acids of ATP13A1 not present in the cDNA construct and the D533A mutations was introduced by Gibson assembly. To modulate induced expression levels (fig. S9A), the Promega-series CMV*d1* truncation was generated in pcDNA5/FRT/TO expression vectors using conventional molecular biology techniques. ATP13A1 coding sequences were transferred from pcDNA5 to pcDNA3.1-based vectors behind 3xFLAG and 3xHA tags for transient transfection (e.g. Fig. 2D) by restriction enzyme digestion and T4 ligation. pOG44 (ThermoFisher V600520) and pX459 (48) are as previously described. Guide RNA sequences (GAG CAC CGT CCC ATA CCC GG, ACG CGC TCA CTG TCC TCT CG) were cloned into pX459 for generating knockout cells using Gibson assembly.

Homemade rabbit polyclonal antibodies against TRAPα [1:5000 for immunoblotting; 1:300 for IF], GFP [1:5000 for IB], and 3F4 [1:350 for IP] were gifts from the Hegde lab. Antibodies against TOM20 (Abcam ab186735) [1:5000 for IB, 1:300 for IF], TOM20 (Santa Cruz sc-17764; RRID:AB_628381) [1:50 for IF], ATP13A1 (ProteinTech 16244-1-AP; RRID:AB_2290293) [1:5000 for IB], FLAG M2 (Sigma F1804; RRID:AB_262044) [1:5000 for IB; 1:500 for IF], CNX (Enzo Life Sciences ADI-SPA-865; RRID:AB_10618434) [1:5000 for IB], Por1 (Abcam ab110326; RRID:AB_10865182) [1:2500 for IB], ATAD1 (Abcam ab94583; RRID:AB_10672816) [1:1000 for IB], DNAJB11 (Proteintech 15484-1-AP; RRID:AB_2094400) [1:2000 for IB], MAVS (Cell Signaling Technology 3993; RRID:AB_823565) [1:1000 for IB]; OMP25 (Abcam ab224217) [1:50 for IF]; OMP25 (ProteinTech 15666-1-AP; RRID:AB_2201149) [1:1000 for IB]; RMDN3 (Thermo Fisher PA5-52680; RRID:AB_2646594) [1:1000 for IB; 1:100 for IF] are commercially available. For immunoblotting, HRP-conjugated anti-mouse (Jackson ImmunoResearch 115-035-003; RRID:AB_10015289) and anti-rabbit (Jackson ImmunoResearch 111-035-003;

RRID:AB_2313567) antibodies were used at 1:5000. For immunofluorescence, AlexaFluor 488-conjugated goat anti-mouse IgG (Jackson ImmunoResearch 115-545-003; RRID:AB_2338840), AlexaFluor 564-conjugated goat anti-rabbit IgG secondary antibodies (Jackson ImmunoResearch 111-585-003; RRID:AB_2338059), and DyLight 680-conjugated anti-HA antibody (ThermoFisher 26183-D680; RRID:AB_2533054) are commercially available.

Yeast strains

BY4741 and Spf1-GFP (e.g. Fig. 1D) yeast strains used for membrane preparations and crosslinking analyses (Fig. 1 and fig. S1) were obtained from the Finley lab (Harvard Medical School). To tag endogenous Spf1 with a 3xFLAG tag (e.g. Fig. 1E), a DNA fragment containing coding sequence for a linker (GSGGRIPGLINM), 3xFLAG, and a hygromycin resistance marker flanked by 50-60-bp homologous to the 3' regions of *SFP1*, was generated by PCR using the pFA-6a-3xFLAG-Hyg plasmid (a gift from P.Feng, Harvard Medical School) as a template and a pair of primers (forward: 5'-caaa cc atc aga cat ttc tgt gca aca ggt caa gat tgc ctc taa agg atc cgg agg acG GAT CCC CGG GTT AAT TAA-3'; reverse: 5'- ggg taa tat aag tat ata aat aca aaa agg ggt act aca taa aag att taG AAT TCG AGC TCG TTT AAA CTG-3'; lowercase and uppercase, specific to the chromosomal and template sequences, respectively). DNA was introduced to BY4741 by a standard lithium acetate transformation protocol before selection with 100 μg/mL hygromycin in YPD agar. Successful FLAG tagging and protein size was confirmed by immunoblotting and Sanger sequencing.

To enable affinity purification of endogenous Spf1 from *S. cerevisiae*, a cleavable GFP-tag was introduced to the 3' end of the *SPF1* coding sequence of the WT strain BY4741. First, a DNA fragment containing a coding sequence for GFP and a nourseothricin resistance marker, which is flanked by ~60-bp sequences homologous to the 3' regions of *SFP1*, was generated by PCR using the pSK-B399 plasmid (a gift from S. Klinge, Rockefeller University) as a template and a pair of primers (forward: 5'-c ttc atg gac gac aaa cca tca gac att tct gtg caa cag gtc aag att gcc tct aaa GGG GCA ACT GGT GGT AG-3'; reverse: 5'-a ctt aga agc tgt ttt aca aat aat aca gca ctt tca taa actt aac aat aca ccc CGG CGT TAG TAT CGA ATC G-3'; lowercase and uppercase, specific to the chromosomal and template sequences, respectively). The DNA segment also contains a 31-amino-acid-long protease-cleavable linker (GATGGSTAGGATTASGTG ENLYFQG TASGGG; underlined, a Tobacco etch virus (TEV) protease cleavage site) between the last codon of *SPF1* and the first codon of GFP. DNA was then introduced to BY4741 by a standard lithium acetate transformation protocol. Transformants were isolated from a YPD agar medium (1% yeast extract, 2% peptone, 2% glucose, and 2% bacto-agar) containing 100 μg/mL nourseothricin. Correct chromosomal integration was confirmed by PCR and Sanger sequencing.

Protein purification for biochemical assays

To purify TA(Bpa) in complex with calcium-calmodulin (CaM), BL21(DE3) cells were co-transformed with pGEX-CaM-FLAG-OMP25(amb) and pEVOL-Bpa and grown in LB under appropriate antibiotic selection to an OD_{600} of 0.6. The cultures were then supplemented with 1 mM Bpa (Bachem 4017646) and induced with 1% arabinose and 0.2

mM IPTG for 6 hr at 25°C. Cells were harvested and resuspended in ice cold lysis buffer [1x PBS, 0.5 mM CaCl$_2$, 1 mM DTT, 1x protease inhibitor cocktail (PIC; Sigma 5056489001)] and lysed by passing through a microfluidizer two times. Soluble material after centrifugation at 34,541g for 20 min in a SS34 rotor (Sorvall) was applied to 1 mL packed glutathione sepharose (GE Life Sciences 17075601) resin equilibrated in lysis buffer per L culture. Columns were washed with 10 column volumes of lysis buffer and eluted with 50 mM Tris (pH 8), 25 mM reduced glutathione, 0.5 mM CaCl$_2$. Peak elution fractions were pooled and dialyzed against 50 mM HEPES (pH 7.4), 150 mM KOAc, 2 mM Mg(OAc)$_2$, 10% glycerol, 1 mM DTT, 0.5 mM CaCl$_2$ for 2 hr before the addition of 1:100 w/w GST-3C protease and dialysis against fresh buffer for 12-16 hr. Dialyzed material was passed over glutathione sepharose column to subtract cleaved GST and GST-3C before being aliquoted and frozen in liquid nitrogen. SGTA, GST-3C protease, and Bpa-RS were expressed in BL21(DE3) *E. coli* and purified as described (24, 46).

Preparation of yeast membranes

Yeast strains were grown in YPG to an OD$_{600}$ of 2, harvested, and washed in distilled water, resuspended in 100 mM Tris-H$_2$SO$_4$ (pH 9.4), 10 mM DTT and incubated at 30°C for 20 min. Cells were then washed in zymolyase buffer [20 mM potassium phosphate (pH 7.4), 1.2 M sorbitol], resuspended in zymolyase buffer containing 3 mg of zymolyase per g cells and incubated at 30°C for 30 min. After another wash in zymolyase buffer, cells were lysed in ice cold homogenization buffer [10 mM Tris-HCl (pH 7.4), 0.6 M sorbitol, 1 mM EDTA, 1 mM PMSF, 0.2% BSA] using a pre-chilled glass-Teflon dounce homogenizer. One volume of homogenization buffer was added and the mixture centrifuged at 1,500g for 5 min. The supernatant was centrifuged at 4,000g for 5 min and again at 12,000g for 15 min. The pellet from the 12,000g spin was resuspended in SEM buffer [20 mM MOPS-KOH (pH 7.2), 250 mM sucrose] and layered on top of a step gradient of: 60%, 32%, 23% and 15% sucrose in 10 mM MOPS-KOH (pH 7.2). Crude membranes were centrifuged at 134,000g for 1 hr in a SW 40Ti rotor, and mitochondria-enriched membranes were collected from the 32%/60% sucrose boundary. The membranes were adjusted to 20-25 mg/mL protein as measured after solubilization in 1% SDS, aliquoted, and frozen in liquid nitrogen. ER-enriched membranes were obtained by centrifuging the post-12,000g supernatant at 234,787g for 45 min in a Type 45 Ti rotor. The pellet was resuspended in RM buffer [50 mM HEPES (pH 7.5), 100 mM KOAc, 2.5 mM Mg(OAc)$_2$, 14% glycerol, 1 mM DTT, 1x PIC], adjusted to ~50 mg/mL protein, aliquoted, and flash frozen in liquid nitrogen. Note that all membrane fractions showed crosslinking to Spf1 due to residual ER contamination in the mitochondria-enriched membrane fractions.

Photocrosslinking of recombinant TA with yeast membranes

Reactions were performed in import buffer [50 mM HEPES (pH 7.5), 100 mM KOAc, 2.5 mM Mg(OAc)$_2$, 0.5 mM CaCl$_2$] containing 7.5-20 μg/mL FLAG-TA(Bpa) in complex with CaM and 5 mg/mL mitochondria-enriched membranes. FLAG-TA(Bpa) was released from CaM by addition of 2 mM EGTA and the samples transferred to a pre-chilled 96-well plate ~10 cm under a UVP B-100 series lamp for 10 min. Ten volumes of IP buffer [50 mM HEPES (pH 7.5), 100 mM KOAc, 2.5 mM Mg(OAc)$_2$, 1% Triton X-100, 1x PIC] were added to each well, and the samples were incubated on ice for 10 min to solubilize

membranes and centrifuged at 21,000g for 5 min. The supernatant was added to M2 anti-FLAG affinity resin (Sigma A2220) and mixed at 4°C for 2 hr. M2 FLAG beads were washed twice with IP buffer, twice with IP buffer + 0.5 M NaCl, and another two times with IP buffer. Elutions were carried out with 0.15 mg/mL 3x FLAG peptide in IP buffer at 30°C for 20 min. Samples for TMT mass spectrometry analysis were treated with 10 mM DTT at 55°C for 30 min, followed by 50 mM chloroacetamide at 25°C in the dark for 20 min. For immunoblotting, elutions were precipitated by addition of one fifth the elution volume of trichloroacetic acid, incubated on ice for 15 min and centrifuged at 21,000g for 1 min. The pellet was washed twice with ice cold acetone and resuspended in protein sample buffer.

Generation of knockout and stable inducible cell lines

All cell lines were maintained in Dulbecco's Modified Eagle's Medium (DMEM) with high glucose, GlutaMAX, and sodium pyruvate (ThermoFisher 10569) with 10% fetal bovine serum (FBS) at 37°C and 5% CO_2. Parent HEK293T, Flp-In T-REx 293, and HeLa T-REx cell lines were authenticated by STR profiling. ATP13A1 knockout cell lines were generated by transfecting Flp-In T-REx HeLa (Fig. 2D and fig. S5-9) or Flp-In T-REx 293 (Fig. 2A-C and fig. S3-4) cells with pX459 plasmids containing target guide RNAs using Lipofectamine 2000 or TransIT293 (Mirus Bio), respectively, according to manufacturer's instructions. After 24 hr, transfected cells were selected with 2 mg/mL puromycin for 48 hr. Single clones were isolated and knockouts validated by immunoblotting and amplicon sequencing.

To establish stable doxycycline-inducible cell lines expressing either FLAG-tagged tail-anchored proteins or FLAG-tagged ATP13A1, wildtype or ATP13A1 knockout Flp-In T-REx HeLa or 293 cells were co-transfected with a 1:1 ratio of pOG44 and pcDNA5/FRT/TO vector containing the desired insert using Lipofectamine 2000/Lipofectamine 3000 or TransIT293 (Mirus Bio), respectively. After 24 hr, cells were selected with 10 μg/mL Blasticidin and 150-300 μg/mL Hygromycin for at least two weeks, and expression was validated by induction with 10 ng/mL doxycycline for 24-48 hr and immunoblotting.

Isolation of rough microsomes

Rough microsomes (RMs) were isolated from wildtype, ATP13A1 KO, and ATP13A1 KO Flp-In T-REx 293 cells stably re-expressing FLAG-tagged WT or D533A ATP13A1 essentially as described (42). Cells were cultured for at least 2 passages in antibiotic-free media. Re-expression of approximately endogenous levels of FLAG-ATP13A1 in the rescue lines (fig. S3A) was achieved by trace levels of tetracycline present in the FBS in the culture media, and no additional doxycycline was added. Cells were harvested and washed twice in cold PBS, and centrifuged at 500g for 5 min. The cell pellet was resuspended in 3 volumes of 10 mM Hepes (pH 7.4), 250 mM sucrose, 2 mM $MgCl_2$, and 1x PIC, and lysed by 25-30 passages through a 27-gauge needle. Lysates were centrifuged twice at 3,800g for 30 min, and the supernatant centrifuged at 75,000g for 1 hr at 4°C in a TLA-55 or TLA-100.3 rotor. The RM pellet was resuspended in 10 mM Hepes (pH 7.4), 250 mM sucrose, 1 mM $MgCl_2$, 0.5 mM DTT, adjusted and normalized to an A_{280} value of 30-60 as measured after solubilization in 1% SDS, and used directly for insertion and extraction assays.

In vitro translation, insertion, extraction, and photocrosslinking

For most in vitro transcription reactions, linear DNA templates were generated by PCR reactions of SP64-based vectors using primers annealing slightly upstream of the SP6 promoter and ~200 bp downstream of the open reading frame. Linear DNA templates for transcribing different C-terminal domain sequences (Fig. 1E) were generated using reverse primers containing the desired C-terminal sequence and 16 bp downstream of the TGA stop codon as follows: TGA GAA TTC CTA ATC ATG TC. DNA templates for testing type II constructs (fig. S10H) were generated by PCR reactions directly from gBlocks (IDT) containing the SP6 promoter, the desired protein-coding sequence, and 16 bp downstream of the stop codon as above. In vitro transcription reactions were performed with SP6 polymerase as described (47) for 1 hr at 37°C and used directly for in vitro translation. Suppressor tRNA (e.g. Fig. 1E) was transcribed from BstN1-lineared plasmid with T7 polymerase at 37°C for 1 hr and isolated by phenol:chloroform extraction. Translation reactions were performed as described (47) at 32°C for 20-30 min. For photocrosslinking, translation reactions were supplemented with an amber suppression system (46) comprised of 5 μM in vitro transcribed suppressor tRNA, 0.5 mM Bpa, and 0.25 μM Bpa-RS. Reactions for targeting assays (fig. S7) included 40 μM cold methionine in place of ^{35}S-methionine. Translation reactions of TA proteins were stopped by the addition of 50 μg/mL RNaseA before the addition of yeast membranes (final concentration of 2-5 mg/mL) (e.g. Fig. 1E) or 1:10 v/v rough microsomes (RMs) (e.g. Fig. 2A-C). Translation reactions of Type II substrates (fig. S10H) included hRMs.

Insertion reactions with yeast membranes were at 25°C for 20 min. For UV-activated crosslinking, insertion reactions were diluted 10-fold in PSB [50 mM HEPES (pH 7.5), 100 mM KOAc, 2.5 mM Mg(OAc)$_2$] and placed ~10 cm under a UVP B-100 series lamp for 10 min in a pre-chilled ice block. SDS was added to a final concentration of 1% and samples were heated to 65°C for 5 min. Ten volumes of IP buffer and 10 μL packed M2 anti-FLAG resin were added, and samples were incubated at 4°C for 1 hr. M2 beads were washed four times in IP buffer before the addition of protein sample buffer. For carbonate extractions (fig. S1B), membranes from 4 μL of insertion reactions were pelleted by centrifugation over a 15% sucrose cushion in PSB at 10,000g for 10 min at 4°C, resuspended in 150 μL 100 mM NaCO$_3$ (pH 11.3), and incubated on ice for 15 min. Samples were centrifuged at 131,440g for 15 min in a TLA100 rotor and the pellets resuspended in protein sample buffer.

Insertion reactions of TA proteins with human cell RMs were at 32°C for 20 min (Fig. 2B, tot.) or 45 min (fig. S3B-D). For photocrosslinking (e.g. Fig. 1E), reactions were diluted 5-fold with PSB, UV-irradiated, and immunoprecipitated as described above. Cotranslational insertion reactions (fig. S10H) were subjected to denaturing IPs with α3F4 antibodies and Protein A resin (CaptivA). Carbonate extractions (fig. S3D) were performed by the addition of 100 reaction volumes of cold 100 mM NaCO$_3$, pH 11.5, incubation on ice for 25 min, followed by centrifugation at 250,000g for 30 min in a TLA100.3 rotor. Pellets were directly resuspended in protein sample buffer for SDS-PAGE and autoradiography analysis. For analysis of insertion efficiency (fig. S3B,C) and extraction reactions (Fig. 2B,C and fig. S4), RMs were pelleted by centrifugation over 4 reaction volumes of a 20% sucrose cushion in PSB at 186,000g for 20 min at 4°C in a TLA-55 rotor and resuspended in half the initial

reaction volume of PSB. Extraction reactions contained ~20 mg/mL RMs (estimated based on total protein concentration), 1 mg/mL SGTA, and either an energy regenerating system (ERS; 1 mM ATP, 1 mM GTP, 1.2 mM creatine phosphate, 20 μg/mL creatine kinase) or 1 mM ATP, 1 mM AMPPCP, or 0.1 U/μL apyrase as indicated, and incubated at 32°C for 30 min. Samples were directly analyzed before or after centrifugation over a 20% sucrose cushion at 186,000g for 20 min. Chemical crosslinking (Fig. 2C) was with 250 μM BMH (Thermo Scientific 22330) at 4°C for 1 hr and directly quenched with protein sample buffer.

Immunofluorescence assays

Flp-In T-REx HeLa cells were cultured either on 13 mm coverslips or in glass bottom 24- or 48-well plates (Mattek). For assays with cell lines harboring inducible substrates (Fig. 2D and fig. S5-8) and analysis of endogenous substrates (Fig. 2G and fig. S10E,F), TA protein or Flag-ATP13A1 expression was induced with 100 ng/mL doxycycline for 24 hr. For rescue assays with stable reporters, cells in a 24-well glass bottom plate were transiently transfected with 200 ng pcDNA3 containing HA-tagged WT or D533A ATP13A1 using Lipofectamine 3000 according to the manufacturer's instructions 48 hr before analysis. For targeting assays (fig. S7), Flp-In T-REx HeLa cells in a 48-well glass bottom dish were washed twice with PSB and incubated with 200 μg/mL digitonin in PSB for 10 min at 4°C. The cells were washed once with PSB before being incubated with 25 μL in vitro translation reaction of FLAG-β-OMP25 at 32°C for 15 min.

For imaging, all cells were washed twice in PBS and fixed in 4% formaldehyde in PBS for 15 min. Cells were washed once in PBS, permeabilized with 0.1% Triton X-100 in PBS for 5 min, and then incubated at room temperature with blocking solution (10% FBS in PBS) for 1 hr followed by primary antibodies in 10% FBS/PBS 1 hr. After three washes in PBS, cells were incubated with 1:500 fluorophore-conjugated secondary antibodies in 10% FBS/PBS for 1 hr and washed three times in PBS before imaging. For ATP13A1 transfection rescue experiments, cells were incubated with 1:100 DyLight 680-conjugated anti-HA antibody (ThermoFisher 26183-D680) in 10% FBS/PBS for 1 hr at room temperature or overnight at 4°C and washed three times with PBS. 13 mm coverslips were placed onto SlowFade Gold Antifade Mountant (ThermoFisher S36936) and sealed using nail polish. Cells in 24- or 48-well plates were imaged directly in PBS.

All images were collected with a Yokagawa CSU-X1 spinning disk confocal with Spectral Applied Research Aurora Borealis modification on a Nikon Ti motorized inverted microscope equipped with Plan Apo 100x/1.4NA oil immersion objective. Fluorescence was excited with solid state lasers at 488nm (100mW), 561nm (100mW) and 642nm (100mW) and collected using ET525/50m, ET620/60m, or ET700/75m emission filters, respectively. Images were acquired with a Hamamatsu ORCA-ER cooled CCD camera. z-series optical sections were collected with a step-size of 0.5 microns and single sections were selected from approximately the center of the cell. Brightness and contrast were adjusted identically for compared image sets using FIJI.

Background subtraction of immunofluorescence images was performed using the robust Otsu thresholding method (49). A region of interest (ROI) was drawn around each cell in the FLAG channel, and colocalization was assessed in 3D using the ImageJ Coloc2 plugin with

a point spread function of 2 and 25 randomizations. Manders' colocalization coefficients (MCC) (50) (e.g. Fig. 2E) indicate the contribution of FLAG signal above 0 that overlaps with mitochondria normalized to the total FLAG signal within the ROI. Pearson's correlation coefficients (PCC) are shown for correlation of FLAG signal with the signal of the ER marker TRAPα (fig. S6) because of the influence of unreliable thresholding of the diffuse ER signal on MCC values. Nonetheless, both MCC1 and MCC2 values with various thresholding techniques support the trends shown in fig. S6, where SEC61β is unaffected, but mitochondrial TA protein colocalization with the ER marker increases in ATP13A1 KO cells. For rescue experiments by transient transfection (Fig. 2D,E and fig. S5A,B), HA staining was used to identify transfected cells; nontransfected cells were not analyzed. The n of cells and fields of views (in parentheses) analyzed are as follows:

- Fig. 2E OMP25 WT – 14 cells (4 fields of view), KO – 14 (3), KO + WT – 17 (5), KO + D533A – 16 (4)

- fig. S5 BAK1 WT – 18 (5), KO – 18 (6), KO + WT – 35 (10), KO + D533A – 22 (9)

- fig. S6 SEC61β WT – 10 (3), SEC61β KO – 9 (3), BAK1 WT – 8 (3), BAK1 KO – 12 (3), OMP25 WT – 9 (3), OMP25 KO – 7 (3)

- fig. S8C BAK1 WT cont. – 16 (3), WT KD – 15 (5), KO cont. – 25 (5), KO KD – 47 (10)

- fig. S8C OMP25 WT cont. – 11 (3), WT KD – 15 (3), KO cont. – 14 (4), KO KD – 44 (10)

- Fig. 2G endogenous OMP25 WT – 32 (10), KO – 32 (10), KO + WT – 19 (8), KO + D533A – 32 (10)

- fig. S10F endogenous RMDN3 WT – 30 (7), KO – 25 (7), KO + WT – 23 (10), KO + D533A – 25 (8).

To compare the level of in vitro translated or stably expressed tail-anchored protein localized to mitochondria (fig. S7C), FLAG signal within mitochondrial ROIs was quantified from 5 (WT + IVT), 4 (KO + IVT; WT steady state), or 3 (KO steady state) different fields of view. Results were analyzed and plotted using Graphpad Prism, and statistical significance tested with unpaired two-tailed Student's t tests.

Miscellaneous biochemistry and analyses

SDS-PAGE was with 8%, 10%, or 12% Tris-tricine polyacrylamide gels with the BioRad mini-gel electrophoresis system. Transfers to 0.2 μm nitrocellulose membranes and immunoblotting were performed using conventional techniques in 5% milk or BSA in PBS + 0.1% Tween, and imaged on a BioRad ChemiDoc Touch or by exposure to XAR film. Transfers in 25 mM potassium phosphate (fig. S1C) (51) were at 15V for 12 hr at 4°C. For autoradiography, gels were dried on filter paper before phosphorimaging or exposure to MR film. Quantification of autoradiography signal was done using phosphorimaging and ImageQuant (GE Healthcare) or by scanning film and with Image J (NIH). 200 μL 5-25% sucrose gradients (fig. S1A) were performed as previously described (24, 52) by

centrifugation at 55,000 rpm for 2 hr 25 min in a TLS-55 rotor followed by manually collecting 11 fractions.

Classification of candidates identified by quantitative proteomics was initially analyzed by GO enrichment terms and then by manually curating specific annotations in UniProt. Signal sequences were retrieved from UniProt, or for unclearly annotated candidates, predicted using SignalP-5.0. Experimentally validated eukaryotic signal sequences were extracted from SPdb (53), and proline content within the first 10 amino acids (fig. S10G) analyzed using the Biostrings R package and R scripts. RNA extraction and quantitative real-time RT-PCR analyses (fig. S10D) were carried out by Syd Labs, Inc. from frozen cell pellets using the following primers: MAVS Fwd – CAT GCT GGG CAG GTC AGT TA, MAVS Rev – TCA AAG CTA CCC TGG AAC GG, OMP25 Fwd – ACC CTC CAC CCC TGC TAT TC, OMP25 Rev – GGT TTG GGG TGG GTA TCA GTC, ATP13A1 Fwd – GTT CGT CGG CTT CAT TGT GG, ATP13A1 Rev – TGG GAC GCA TTC TGG ATC TC, SRP14 Fwd – ATT GGT CTG TGC TGC ATG GT, SRP14 Rev – TGG GTT GGG AAA GGA ATA AAG AG. SRP14 and ATP13A1 were used as normalization and positive controls.

Purification of *S. cerevisiae* Spf1 for cryo-EM analysis

Yeast cells, whose endogenous Spf1 is tagged with C-terminal TEV-GFP, were grown in YPD medium (1% yeast extract, 2% peptone, and 2% glucose) in shaker flasks at 30 °C to an optical density (OD600) of 2–4. Cells were harvested by centrifugation, frozen in liquid nitrogen, and stored in −80 °C until use. Cells were lysed by cryo-milling and resuspended in buffer containing 50 mM Tris pH 7.5, 200 mM NaCl, 1 mM EDTA, 1 mM DTT, 10% glycerol, 5 μg/ml aprotinin, 5 μg/ml leupeptin, 1 μg/ml pepstatin A, and 2 mM PMSF. All subsequent steps were carried out at 4 °C. To purify apo Spf1, 1% n-Dodecyl-β-D-Maltopyranoside (DDM; Anatrace) and 0.2% cholesteryl hemisuccinate (CHS; Anatrace) were directly added to the cell lysate. After 3-hr solubilization, the lysate was clarified by ultracentrifugation (Beckman Type 45 Ti rotor) at 120,000g for 1hr, and the supernatant was mixed with Sepharose beads conjugated with anti-GFP nanobody for 2.5 hr. The beads were washed with approximately 30 column volumes of a wash buffer (Buffer W) containing 20 mM Tris pH 7.5, 100 mM NaCl, 1 mM EDTA, 1 mM DTT, 0.04% DDM, 0.008% CHS. Spf1 was eluted by incubating the beads with ~10 ug/mL TEV protease (in Buffer W) for ~14 hr. The eluate was concentrated and injected into a Superose 6 Increase column (GE Lifesciences) equilibrated with Buffer W. Peak fractions were pooled and concentrated to ~5 mg/mL before cryo-EM grid preparation. For Spf1 bound to AMP-PCP, AlF$_4$, and BeF$_3$, the running buffer for size-exclusion chromatography additionally contained 10 mM MgCl$_2$, and the purified Spf1 was incubated with either 2 mM of AMP-PCP, AlF$_4$, or BeF$_3$ for 1 hr at 4 °C before grid preparation.

For the substrate-bound structure, the purification procedure was modified as follows. After cryo-milling, unbroken cells and large debris were removed by centrifugation at 4,000g for 10 min. Membranes were pelleted by ultracentrifugation (Beckman Type 45 Ti rotor) at 120,000g for 1.5 hr and resuspended in buffer containing 50 mM Tris pH 7.5, 200 mM NaCl, 1 mM EDTA, 1 mM DTT, 10% glycerol, 2 mM BeF3, 10 mM MgCl$_2$, 5 μg/ml aprotinin, 5 μg/ml leupeptin, 1 μg/ml pepstatin A, and 2 mM PMSF. The membranes were

then solubilized with 1% DDM and 0.2% CHS for 2.5 hr. After clarification by ultracentrifugation, the lysate was incubated with anti-GFP nanobody beads for 3 hr. The beads were then washed with approximately 30 column volumes of Buffer W additionally containing 10 mM $MgCl_2$ and 2 mM BeF_3. After eluting with the TEV protease, purified Spf1 was injected into a Superose 6 column equilibrated with the same wash buffer. Peak fractions were pooled, concentrated to ~5 mg/mL, and immediately used for cryo-EM grid preparation.

Cryo-EM grid preparation and data acquisition

To prepare cryo-EM grids, gold Quantifoil R 1.2/1.3 holey carbon grids were treated with glow discharge for 35 sec using a PELCO easiGlow system (0.39 mBar air, 25 mA). 3 μL of the Spf1 sample were applied to a grid. The grid was blotted for 2–3 s with Grade 1 Whatman filter paper and plunge-frozen in liquid-nitrogen-cooled liquid ethane using Vitrobot Mark IV (FEI) operated at 4° C and 100% humidity.

The apo and AlF_4 datasets were collected on a Talos Arctica electron microscope (FEI) operated at an acceleration voltage of 200 kV, and the other datasets were collected on a Titan Krios electron microscope (FEI) operated at an acceleration voltage of 300 kV and equipped with a Gatan GIF Quantum LS Image Filter (a slit width of 20 eV) (table S1). Dose-fractionated images (~50–60 electrons per $Å^2$ over 42 frames) were recorded on a K3 direct electron detector (Gatan) operated in the super-resolution mode using SerialEM software (54). The physical pixel size was 1.14 Å for apo, 0.90 Å for AlF_4, and 1.19 Å for the other datasets. Target defocus values were from −1.0 μm to −2.4 μm.

Cryo-EM structure determination

The single-particle analysis procedures are described in fig. S11D, S17 B,C, and table S1. First, tile-based motion correction of movies (using 7 by 5 tiles), contrast transfer function (CTF) estimation, and automatic particle picking were performed using Warp (55). During this process, the corrected movies were 2x frame-binned by averaging each two frames, resulting in a total of 21 frames per movie. Micrographs that were not suitable for image analysis (mostly those containing crystalline ice) were removed by manual inspection. All subsequent image processing was performed using cryoSPARC v2 (56) with the particles and 2x-binned movies imported from Warp. Except for the substrate-bound Spf1 dataset, the particles were polished by per-particle motion correction on the 2x-binned movies (57). The dimensions of extracted particle images were 256 pixels (320 pixels for the AlF_4 dataset). The particle images were then subjected to reference-free 2D classification. Most particles discarded by the 2D classification were empty detergent micelle particles. For the AlF_4 and BeF_3 datasets, the first 2D classification was performed before the particle polishing and another 2D classification after the polishing.

These particles were used for generation of three (for apo, AMP-PCP, and AlF_4) or five (for BeF_3- and substrate-bound Spf1) initial models (ab-initio reconstruction), followed by one or two rounds of 3D classification (heterogeneous refinement). For the apo, AMP-PCP, and AlF_4 datasets, only one class (contains ~55-80% particles from the 2D classification) showed features of Spf1, which was used for 3D refinement. In the case of the BeF_3 dataset

(without substrate), a minor class of the apo-like inward-open structure (23% particles) in addition to the major class of the outward-open structure (57% particles) was found in the 3D classification. In the case of the substrate-bound structure, three out of five classes (total 87% particles) showed equally clear Spf1 features with the outward-open conformation, whereas the two other minor classes did show little or no protein densities. All three good classes also showed a clear additional TM helix-like density of a putative endogenous substrate. Because substrate occupancy is likely partial, we subjected particles to a second round of 3D classification using two reference models, one of the three substrate-bound classes containing the substrate density and a structure without a substrate (from outward-open BeF_3-bound structure without a substrate). This resulted in two classes with a stronger (Class A) and weaker (Class B) substrate density, and particles from Class A was used for 3D refinement. Particles from selected classes were refined to the final maps by CTF refinement and non-uniform refinement. The overall resolution was estimated based on gold-standard Fourier shell correlation (FSC) of independently refined half maps and the 0.143 cut-off criterion. Local resolution was estimated in cryoSPARC using default parameters (fig. S12A and S18 M-P). Unless indicated otherwise, the maps shown in figures were sharpened with B-factors estimated in the non-uniform refinement and lowpass-filtered at their resolution.

The initial atomic model was built de novo into the sharpened, lowpass-filtered combined map of the apo Spf1 using Coot (58). Models for the other structures were built using Coot after rigid-body fitting of individual domains (or groups of TM segments) of the apo Spf1 structure into corresponding maps. The following segments were not modeled as they were invisible or poorly resolved in the density maps: N–3, 45–54 (a loop between TMa and TMb), 646–652 (a loop in the N-domain), 853–957 (the arm domain), and 1212–C. In addition, the segments 562–571 (a part of the N-domain), 842–852 (the arm domain), and 958–962 (the connection from the arm domain to the P-domain) were modeled with alanine as we could not unambiguously register amino acids. Model refinement was done in real space using Phenix 1.16 (59) with refinement resolution limit set to the overall resolution of the map. MolProbity (60) and EMRinger (61) in the Phenix package was used for structural validation (table S1). Protein electrostatics were calculated using the Adaptive Poisson-Boltzmann Solver (62, 63) with default parameters built in PyMOL v2.3 (with monovalent ion concentrations of 0.15 M each). Cavities were detected by Hollow (64). UCSF Chimera (65), Chimera X (66), and PyMOL (Schrödinger) were used to prepare structural figures in the paper.

Sample preparation and digestion for mass spectrometry

Protein extracts were subjected to disulfide bond reduction with 5 mM TCEP (room temperature, 10 min) and alkylation with 25 mM chloroacetamide (room temperature, 20 min) followed by methanol–chloroform precipitation (Fig. 2F and fig. S9) or TCA precipitation (Fig. 1C), prior to protease digestion. Samples were resuspended in 100 mM EPPS, pH 8.5 containing 0.1% RapiGest and digested at 37°C for 2 hr with LysC protease at a 200:1 protein-to-protease ratio. Trypsin was then added at a 100:1 protein-to-protease ratio and the reaction was incubated for 6 hr at 37°C. Tandem mass tag labeling of each sample was performed by adding indicated amount of the 20 ng/μL stock of TMT or TMTpro

reagent along with acetonitrile to achieve a final acetonitrile concentration of approximately 30% (v/v). Typically 5 μL of TMTpro reagent was added for 50 μg of protein input (Fig. 2F and fig. S9), 3 μL of TMT reagent for affinity purification samples (Fig. 1C). Following incubation at room temperature for 1 hr, labeling efficiency of a small aliquot was tested, and the reaction was then quenched with hydroxylamine to a final concentration of 0.5% (v/v) for 15 min. The TMT-labeled samples were pooled together at a 1:1 ratio. The sample was vacuum centrifuged to near dryness, resuspended in 5% formic acid for 15 min, centrifuged at 10000×g for 5 min at room temperature and subjected to C18 solid-phase extraction (SPE) (Sep-Pak, Waters).

For whole proteome samples (Fig. 2F and fig. S9), dried TMT-labeled sample was resuspended in 100 μL of 10 mM NH_4HCO_3 pH 8.0 and fractionated using BPRP HPLC (67). Briefly, samples were offline fractionated over a 90 min run, into 96 fractions by high pH reverse-phase HPLC (Agilent LC1260) through an aeris peptide xb-c18 column (Phenomenex; 250 mm x 3.6 mm) with mobile phase A containing 5% acetonitrile and 10 mM NH_4HCO_3 in LC-MS grade H_2O, and mobile phase B containing 90% acetonitrile and 10 mM NH_4HCO_3 in LC-MS grade H_2O (both pH 8.0). The 96 resulting fractions were then pooled in a non-continuous manner into 24 fractions (as outlined in Supplemental Fig. 5 of (67)). Fractions were vacuum centrifuged to near dryness. Each consolidated fraction was desalted via StageTip, dried again via vacuum centrifugation, and reconstituted in 5% acetonitrile, 1% formic acid for LC-MS/MS processing.

Liquid chromatography and tandem mass spectrometry

For UV-crosslinking samples (Fig. 1C), mass spectrometry data were collected using an Orbitrap Fusion Lumos mass spectrometer (Thermo Fisher Scientific, San Jose, CA) coupled to a Proxeon EASY-nLC1200 liquid chromatography (LC) pump (Thermo Fisher Scientific). Peptides were separated on a 100 μm inner diameter microcapillary column packed in house with ~35 cm of Accucore150 resin (2.6 μm, 150 Å, Thermo Fisher Scientific, San Jose, CA) with a gradient consisting of 5%–22% (0-100 min)), 22-28% (100-110min) (ACN, 0.1% FA) over a total 120 min run at ~500 nL/min. Each analysis used the Multi-Notch MS^3-based TMT method (68), to reduce ion interference compared to MS^2 quantification, combined with newly implemented Real Time Search analysis software (69, 70). The scan sequence began with an MS^1 spectrum (Orbitrap analysis; resolution 120,000 at 200 Th; mass range 400–1400 m/z; automatic gain control (AGC) target 1×10^6; maximum injection time 240 ms). Precursors for MS^2 analysis were selected using a 3 sec TopSpeed method. MS^2 analysis consisted of collision-induced dissociation (quadrupole ion trap analysis; Rapid scan rate; AGC 2.5×10^4; isolation window 0.7 Th; normalized collision energy (NCE) 35; maximum injection time 60 ms). Monoisotopic peak assignment was used, and previously interrogated precursors were excluded using a dynamic window (120 s ± 7 ppm). Following acquisition of each MS^2 spectrum, a synchronous-precursor-selection (SPS) API-MS^3 scan was collected on the top 10 most intense ions b or y-ions matched by the online search algorithm in the associated MS^2 spectrum (69, 70) . MS^3 precursors were fragmented by high energy collision-induced dissociation (HCD) and analyzed using the Orbitrap (NCE 65; AGC 2.5×10^5; maximum injection time 200 ms, resolution was 50,000 at

200 Th). Previously identified peptides corresponding to human SEC61B where included in a targeted mass list and given priority for MS^2 and SPS-MS^3.

For whole cell proteome analysis (Fig. 2F and fig. S9), mass spectrometry data were collected using an Orbitrap Fusion Lumos mass spectrometer combined with a high-field asymmetric waveform ion mobility spectrometry (FAIMS) Pro interface, coupled to a Proxeon EASY-nLC1200 liquid chromatography (LC) pump (Thermo Fisher Scientific). Peptides were separated on a 100 μm inner diameter microcapillary column packed in house with ~35 cm of Accucore150 resin (2.6 μm, 150 Å, Thermo Fisher Scientific, San Jose, CA) with a gradient consisting of 5%–15% (0-70 min), 15-23% (70-85min) (ACN, 0.1% FA) over a total 95 min run at ~500 nL/min. For analysis, we loaded 1/3 of each fraction onto the column. To reduce ion interference compared to MS^2 quantification, each analysis used the Multi-Notch MS^3-based TMT method (68), combined with newly implemented Real Time Search analysis software (69, 70) and the FAIMS Pro Interface. The scan sequence began with an MS^1 spectrum (Orbitrap analysis; resolution 120,000 at 200 Th; mass range 400–1600 m/z; automatic gain control (AGC) target 8×10^5; maximum injection time 50 ms). Precursors for MS^2 analysis were selected using a cycle type of 1.25 sec/CV method (FAIMS CV=−40/−60/−80 previously optimized for TMT multiplexed samples (71)). MS^2 analysis consisted of collision-induced dissociation (quadrupole ion trap analysis; Rapid scan rate; AGC 1.0×10^4; isolation window 0.7 Th; normalized collision energy (NCE) 35; maximum injection time 35 ms). Monoisotopic peak assignment was used, precursor fit filter was used (70% for a fit window of 0.7 Th) and previously interrogated precursors were excluded using a dynamic window (120 s ± 10 ppm). Following acquisition of each MS^2 spectrum, a synchronous-precursor-selection (SPS) API-MS^3 scan was collected on the top 10 most intense ions b or y-ions matched by the online search algorithm in the associated MS^2 spectrum (69, 70). MS^3 precursors were fragmented by high energy collision-induced dissociation (HCD) and analyzed using the Orbitrap (NCE 45; AGC 2.5×10^5; maximum injection time 200 ms, resolution was 50,000 at 200 Th).

Proteomics data analysis

Mass spectra were processed using a Comet-based (v2018.01 rev.2) in-house software pipeline (72, 73) or Sequest-HT (for Fig. 1C) using Proteome Discoverer (v2.3.0.420 - Thermo Fisher Scientific).

The identification of UV-crosslinked proteins (Fig. 1C) was performed using the SEQUEST-HT engine (Proteome Discoverer v2.3.0.420 - Thermo Fisher Scientific) against the UniProt Saccharomyces Cerevisiae (S288c) Reference Proteome (07/2017), as well as an in-house curated list of contaminants and the human SEC61B sequence, using the following parameters (post-recalibration): a tolerance level of 10 ppm for MS^1 and 0.7 Da for MS^2 and false discovery rate of the Percolator decoy database search was set to 1%. Trypsin and LysC were used as the digestion enzymes, two missed cleavages were allowed, and the minimal peptide length was set to 7 amino acids. TMT tags on lysine residues and peptide N termini (+229.163 Da) and carbamidomethylation of cysteine residues (+57.021 Da) were set as static modifications, while oxidation of methionine residues (+15.995 Da) was set as a variable modification. For TMT-based reporter ion quantitation, we extracted (integration

tolerance of 0.003 Da) the summed signal-to-noise ratio for each TMT channel and found the closest matching centroid to the expected mass of the TMT reporter ion. For protein-level comparisons, PSMs were identified, quantified, and collapsed to a 1% peptide false discovery rate (FDR) and then collapsed further to a final protein-level FDR of 1%. Moreover, protein assembly was guided by principles of parsimony to produce the smallest set of proteins necessary to account for all observed peptides. Proteins were quantified by summing reporter ion counts across all matching PSMs for unique peptides only. PSMs with poor quality, MS^3 spectra with TMT reporter summed signal-to-noise ratio that were less than 10 per channel, isolation specificity 0.2, or had less than 70% of correctly selected SPS ions were excluded from quantification.

For whole proteome analysis (Fig. 2F and fig. S9), spectra were converted to mzXML using a modified version of ReAdW.exe. Database searching included all canonical entries from the human Reference Proteome UniProt database (SwissProt – 2019-01), as well as an in-house curated list of contaminants. This database was concatenated with one composed of all protein sequences in the reversed order. Trypsin was used as the digestion enzyme, two missed cleavages were allowed, and the minimal peptide length was set to 7 amino acids. Searches were performed using a 20 ppm precursor ion tolerance for total protein level analysis. The recommended product ion parameters for ion trap ms/ms were used (1.0005 tolerance, 0.4 offset (mono masses), theoretical_fragment_ions = 1). TMTpro tags on lysine residues and peptide N termini (+304.2071 Da) and carbamidomethylation of cysteine residues (+57.021 Da) were set as static modifications, while oxidation of methionine residues (+15.995 Da) was set as a variable modification. Peptide-spectrum matches (PSMs) were adjusted to a 1% false discovery rate (FDR) and PSM filtering was performed using a linear discriminant analysis, as described previously (73), while considering the following parameters: Comet Log Expect and Diff Seq. Delta Log Expect, missed cleavages, peptide length, charge state, and precursor mass accuracy. For TMT-based reporter ion quantitation, we extracted the summed signal-to-noise (S:N) ratio for each TMT channel and found the closest matching centroid to the expected mass of the TMT reporter ion (integration tolerance of 0.003 Da). For protein-level comparisons, PSMs were identified, quantified, and collapsed to a 1% peptide false discovery rate (FDR) and then collapsed further to a final protein-level FDR of 1%. Moreover, protein assembly was guided by principles of parsimony to produce the smallest set of proteins necessary to account for all observed peptides. Proteins were quantified by summing reporter ion counts across all matching PSMs using in-house software, as described previously (73). PSMs with poor quality, MS3 spectra with more than 6 TMTpro reporter ion channels missing, or isolation specificity less than 0.6, or with TMT reporter summed signal-to-noise ratio that were less than 200 or had no MS3 spectra were excluded from quantification.

Protein quantification values were exported for further analysis in Microsoft Excel and Perseus (74) and statistical test and parameters used are indicated in the corresponding datasets (Data S1 and S2). Briefly, Welch's t-test analysis was performed to compare two datasets, using s0 parameter (in essence a minimal fold change cut-off) and correction for multiple comparison was achieved by the permutation-based FDR method, both functions that are built-in in Perseus software. For whole cell proteome (Fig. 2F and fig. S9) analysis, each reporter ion channel was summed across all quantified proteins and normalized

assuming equal protein loading of all 16 samples. For affinity-purified samples (Fig. 1C) normalization based on SEC61B (total TMT sum signal to noise) was performed.

Supplementary Material

Refer to Web version on PubMed Central for supplementary material.

Acknowledgements:

References and Notes

1. Costa EA, Subramanian K, Nunnari J, Weissman JS, Defining the physiological role of SRP in protein-targeting efficiency and specificity. Science 359, 689–692 (2018). [PubMed: 29348368]

2. Gamerdinger M, Hanebuth MA, Frickey T, Deuerling E, The principle of antagonism ensures protein targeting specificity at the endoplasmic reticulum. Science 348, 201–207 (2015). [PubMed: 25859040]

3. Chio US, Cho H, Shan SO, Mechanisms of Tail-Anchored Membrane Protein Targeting and Insertion. Annu Rev Cell Dev Biol 33, 417–438 (2017). [PubMed: 28992441]

4. Krumpe K et al., Ergosterol content specifies targeting of tail-anchored proteins to mitochondrial outer membranes. Mol Biol Cell 23, 3927–3935 (2012). [PubMed: 22918956]

5. Dyla M, Kjaergaard M, Poulsen H, Nissen P, Structure and Mechanism of P-Type ATPase Ion Pumps. Annu Rev Biochem, 10.1146/annurev-biochem-010611-112801 (2019).

6. Andersen JP et al., P4-ATPases as Phospholipid Flippases-Structure, Function, and Enigmas. Front Physiol 7, 275 (2016). [PubMed: 27458383]

7. Sorensen DM, Buch-Pedersen MJ, Palmgren MG, Structural divergence between the two subgroups of P5 ATPases. Biochim Biophys Acta 1797, 846–855 (2010). [PubMed: 20416272]

8. van Veen S et al., ATP13A2 deficiency disrupts lysosomal polyamine export. Nature 578, 419–424 (2020). [PubMed: 31996848]

9. Sorensen DM et al., Parkinson disease related ATP13A2 evolved early in animal evolution. PLoS One 13, e0193228 (2018). [PubMed: 29505581]

10. Cronin SR, Rao R, Hampton RY, Cod1p/Spf1p is a P-type ATPase involved in ER function and Ca2+ homeostasis. J Cell Biol 157, 1017–1028 (2002). [PubMed: 12058017]

11. Dederer V et al., Cooperation of mitochondrial and ER factors in quality control of tail-anchored proteins. Elife 8, 10.7554/eLife.45506 (2019).

12. Suzuki C, Shimma YI, P-type ATPase spf1 mutants show a novel resistance mechanism for the killer toxin SMKT. Mol Microbiol 32, 813–823 (1999). [PubMed: 10361284]

13. Sorensen DM et al., The P5A ATPase Spf1p is stimulated by phosphatidylinositol 4-phosphate and influences cellular sterol homeostasis. Mol Biol Cell 30, 1069–1084 (2019). [PubMed: 30785834]

14. Cronin SR, Khoury A, Ferry DK, Hampton RY, Regulation of HMG-CoA reductase degradation requires the P-type ATPase Cod1p/Spf1p. J Cell Biol 148, 915–924 (2000). [PubMed: 10704442]

15. Vashist S, Frank CG, Jakob CA, Ng DT, Two distinctly localized p-type ATPases collaborate to maintain organelle homeostasis required for glycoprotein processing and quality control. Mol Biol Cell 13, 3955–3966 (2002). [PubMed: 12429838]

16. Ando A, Suzuki C, Cooperative function of the CHD5-like protein Mdm39p with a P-type ATPase Spf1p in the maintenance of ER homeostasis in Saccharomyces cerevisiae. Mol Genet Genomics 273, 497–506 (2005). [PubMed: 15909163]

17. Jonikas MC et al., Comprehensive characterization of genes required for protein folding in the endoplasmic reticulum. Science 323, 1693–1697 (2009). [PubMed: 19325107]

18. Cohen Y et al., The yeast p5 type ATPase, spf1, regulates manganese transport into the endoplasmic reticulum. PLoS One 8, e85519 (2013). [PubMed: 24392018]

19. Suzuki C, Immunochemical and mutational analyses of P-type ATPase Spf1p involved in the yeast secretory pathway. Biosci Biotechnol Biochem 65, 2405–2411 (2001). [PubMed: 11791712]

20. Tipper DJ, Harley CA, Yeast genes controlling responses to topogenic signals in a model transmembrane protein. Mol Biol Cell 13, 1158–1174 (2002). [PubMed: 11950929]

21. Sorensen DM, Holen HW, Holemans T, Vangheluwe P, Palmgren MG, Towards defining the substrate of orphan P5A-ATPases. Biochim Biophys Acta 1850, 524–535 (2015). [PubMed: 24836520]

22. Shao S, Hegde RS, A calmodulin-dependent translocation pathway for small secretory proteins. Cell 147, 1576–1588 (2011). [PubMed: 22196732]

23. Guna A, Volkmar N, Christianson JC, Hegde RS, The ER membrane protein complex is a transmembrane domain insertase. Science 359, 470–473 (2018). [PubMed: 29242231]

24. Shao S, Rodrigo-Brenni MC, Kivlen MH, Hegde RS, Mechanistic basis for a molecular triage reaction. Science 355, 298–302 (2017). [PubMed: 28104892]

25. Wiedemann N, Pfanner N, Mitochondrial Machineries for Protein Import and Assembly. Annu Rev Biochem 86, 685–714 (2017). [PubMed: 28301740]

26. Chen YC et al., Msp1/ATAD1 maintains mitochondrial function by facilitating the degradation of mislocalized tail-anchored proteins. EMBO J 33, 1548–1564 (2014). [PubMed: 24843043]

27. Martensson CU et al., Mitochondrial protein translocation-associated degradation. Nature 569, 679–683 (2019). [PubMed: 31118508]

28. Wohlever ML, Mateja A, McGilvray PT, Day KJ, Keenan RJ, Msp1 Is a Membrane Protein Dislocase for Tail-Anchored Proteins. Mol Cell 67, 194–202 e196 (2017). [PubMed: 28712723]

29. Okreglak V, Walter P, The conserved AAA-ATPase Msp1 confers organelle specificity to tail-anchored proteins. Proc Natl Acad Sci U S A 111, 8019–8024 (2014). [PubMed: 24821790]

30. Matsumoto S et al., Msp1 Clears Mistargeted Proteins by Facilitating Their Transfer from Mitochondria to the ER. Mol Cell 76, 191–205 e110 (2019). [PubMed: 31445887]

31. Park E, Rapoport TA, Mechanisms of Sec61/SecY-mediated protein translocation across membranes. Annu Rev Biophys 41, 21–40 (2012). [PubMed: 22224601]

32. Hegde RS, Bernstein HD, The surprising complexity of signal sequences. Trends Biochem Sci 31, 563–571 (2006). [PubMed: 16919958]

33. Toyoshima C, Nakasako M, Nomura H, Ogawa H, Crystal structure of the calcium pump of sarcoplasmic reticulum at 2.6 A resolution. Nature 405, 647–655 (2000). [PubMed: 10864315]

34. Sorensen TL, Moller JV, Nissen P, Phosphoryl transfer and calcium ion occlusion in the calcium pump. Science 304, 1672–1675 (2004). [PubMed: 15192230]

35. Morth JP et al., Crystal structure of the sodium-potassium pump. Nature 450, 1043–1049 (2007). [PubMed: 18075585]

36. Abe K, Irie K, Nakanishi H, Suzuki H, Fujiyoshi Y, Crystal structures of the gastric proton pump. Nature 556, 214–218 (2018). [PubMed: 29618813]

37. Bublitz M, Poulsen H, Morth JP, Nissen P, In and out of the cation pumps: P-type ATPase structure revisited. Curr Opin Struct Biol 20, 431–439 (2010). [PubMed: 20634056]

38. Timcenko M et al., Structure and autoregulation of a P4-ATPase lipid flippase. Nature 571, 366–370 (2019). [PubMed: 31243363]

39. Hiraizumi M, Yamashita K, Nishizawa T, Nureki O, Cryo-EM structures capture the transport cycle of the P4-ATPase flippase. Science 365, 1149–1155 (2019). [PubMed: 31416931]

40. Bai L et al., Autoinhibition and activation mechanisms of the eukaryotic lipid flippase Drs2p-Cdc50p. Nat Commun 10, 4142 (2019). [PubMed: 31515475]

41. Hansen KG et al., An ER surface retrieval pathway safeguards the import of mitochondrial membrane proteins in yeast. Science 361, 1118–1122 (2018). [PubMed: 30213914]

42. Chitwood PJ, Juszkiewicz S, Guna A, Shao S, Hegde RS, EMC Is Required to Initiate Accurate Membrane Protein Topogenesis. Cell 175, 1507–1519 e1516 (2018). [PubMed: 30415835]

43. Volkmar N, Christianson JC, Squaring the EMC - how promoting membrane protein biogenesis impacts cellular functions and organismal homeostasis. J Cell Sci 133, (2020).

44. Itakura E et al., Ubiquilins Chaperone and Triage Mitochondrial Membrane Proteins for Degradation. Mol Cell 63, 21–33 (2016). [PubMed: 27345149]

45. Chin JW, Martin AB, King DS, Wang L, Schultz PG, Addition of a photocrosslinking amino acid to the genetic code of Escherichiacoli. Proc Natl Acad Sci U S A 99, 11020–11024 (2002). [PubMed: 12154230]

46. Lin Z et al., TTC5 mediates autoregulation of tubulin via mRNA degradation. Science 367, 100–104 (2020). [PubMed: 31727855]

47. Feng Q, Shao S, In vitro reconstitution of translational arrest pathways. Methods 137, 20–36 (2018). [PubMed: 29277545]

48. Ran FA et al., Genome engineering using the CRISPR-Cas9 system. Nat Protoc 8, 2281–2308 (2013). [PubMed: 24157548]

49. Otsu N, A threshold selection method from gray-level histograms. IEEE Trans Sy. Man Cyber 9, 62–66 (1979).

50. Manders EMM, Verbeek FJ, Aten JA, Measurement of co-localization of objects in dual-colour confocal images. Journal of Microscopy 169, 375–382 (1993).

51. Hincke MT, Conditions for improved adsorption of calmodulin to nitrocellulose: detection by 45Ca binding. Electrophoresis 9, 303–306 (1988). [PubMed: 3234368]

52. Yip MCJ et al., Mechanism for recycling tRNAs on stalled ribosomes. Nat Struct Mol Biol 26, 343–349 (2019). [PubMed: 31011209]

53. Choo KH, Tan TW, Ranganathan S, SPdb--a signal peptide database. BMC Bioinformatics 6, 249 (2005). [PubMed: 16221310]

54. Mastronarde DN, Automated electron microscope tomography using robust prediction of specimen movements. J Struct Biol 152, 36–51 (2005). [PubMed: 16182563]

55. Tegunov D, Cramer P, Real-time cryo-electron microscopy data preprocessing with Warp. Nat Methods 16, 1146–1152 (2019). [PubMed: 31591575]

56. Punjani A, Rubinstein JL, Fleet DJ, Brubaker MA, cryoSPARC: algorithms for rapid unsupervised cryo-EM structure determination. Nat Methods 14, 290–296 (2017). [PubMed: 28165473]

57. Rubinstein JL, Brubaker MA, Alignment of cryo-EM movies of individual particles by optimization of image translations. J Struct Biol 192, 188–195 (2015). [PubMed: 26296328]

58. Emsley P, Lohkamp B, Scott WG, Cowtan K, Features and development of Coot. Acta Crystallogr D Biol Crystallogr 66, 486–501 (2010). [PubMed: 20383002]

59. Afonine PV et al., Real-space refinement in PHENIX for cryo-EM and crystallography. Acta Crystallogr D Struct Biol 74, 531–544 (2018). [PubMed: 29872004]

60. Chen VB et al., MolProbity: all-atom structure validation for macromolecular crystallography. Acta Crystallogr D Biol Crystallogr 66, 12–21 (2010). [PubMed: 20057044]

61. Barad BA et al., EMRinger: side chain-directed model and map validation for 3D cryo-electron microscopy. Nat Methods 12, 943–946 (2015). [PubMed: 26280328]

62. Baker NA, Sept D, Joseph S, Holst MJ, McCammon JA, Electrostatics of nanosystems: application to microtubules and the ribosome. Proc Natl Acad Sci U S A 98, 10037–10041 (2001). [PubMed: 11517324]

63. Dolinsky TJ, Nielsen JE, McCammon JA, Baker NA, PDB2PQR: an automated pipeline for the setup of Poisson-Boltzmann electrostatics calculations. Nucleic Acids Res 32, W665–667 (2004). [PubMed: 15215472]

64. Ho BK, Gruswitz F, HOLLOW: generating accurate representations of channel and interior surfaces in molecular structures. BMC Struct Biol 8, 49 (2008). [PubMed: 19014592]

65. Pettersen EF et al., UCSF Chimera--a visualization system for exploratory research and analysis. J Comput Chem 25, 1605–1612 (2004). [PubMed: 15264254]

66. Goddard TD et al., UCSF ChimeraX: Meeting modern challenges in visualization and analysis. Protein Sci 27, 14–25 (2018). [PubMed: 28710774]

67. Paulo JA et al., Quantitative mass spectrometry-based multiplexing compares the abundance of 5000 S. cerevisiae proteins across 10 carbon sources. J Proteomics 148, 85–93 (2016). [PubMed: 27432472]

68. McAlister GC et al., MultiNotch MS3 enables accurate, sensitive, and multiplexed detection of differential expression across cancer cell line proteomes. Anal Chem 86, 7150–7158 (2014). [PubMed: 24927332]

69. Erickson BK et al., Active Instrument Engagement Combined with a Real-Time Database Search for Improved Performance of Sample Multiplexing Workflows. J Proteome Res 18, 1299–1306 (2019). [PubMed: 30658528]

70. Schweppe DK et al., Full-Featured, Real-Time Database Searching Platform Enables Fast and Accurate Multiplexed Quantitative Proteomics. J Proteome Res, 10.1021/acs.jproteome.1029b00860 (2020).

71. Schweppe DK et al., Characterization and Optimization of Multiplexed Quantitative Analyses Using High-Field Asymmetric-Waveform Ion Mobility Mass Spectrometry. Anal Chem 91, 4010–4016 (2019). [PubMed: 30672687]

72. Eng JK, Jahan TA, Hoopmann MR, Comet: an open-source MS/MS sequence database search tool. Proteomics 13, 22–24 (2013). [PubMed: 23148064]

73. Huttlin EL et al., A tissue-specific atlas of mouse protein phosphorylation and expression. Cell 143, 1174–1189 (2010). [PubMed: 21183079]

74. Tyanova S et al., The Perseus computational platform for comprehensive analysis of (prote)omics data. Nat Methods 13, 731–740 (2016). [PubMed: 27348712]
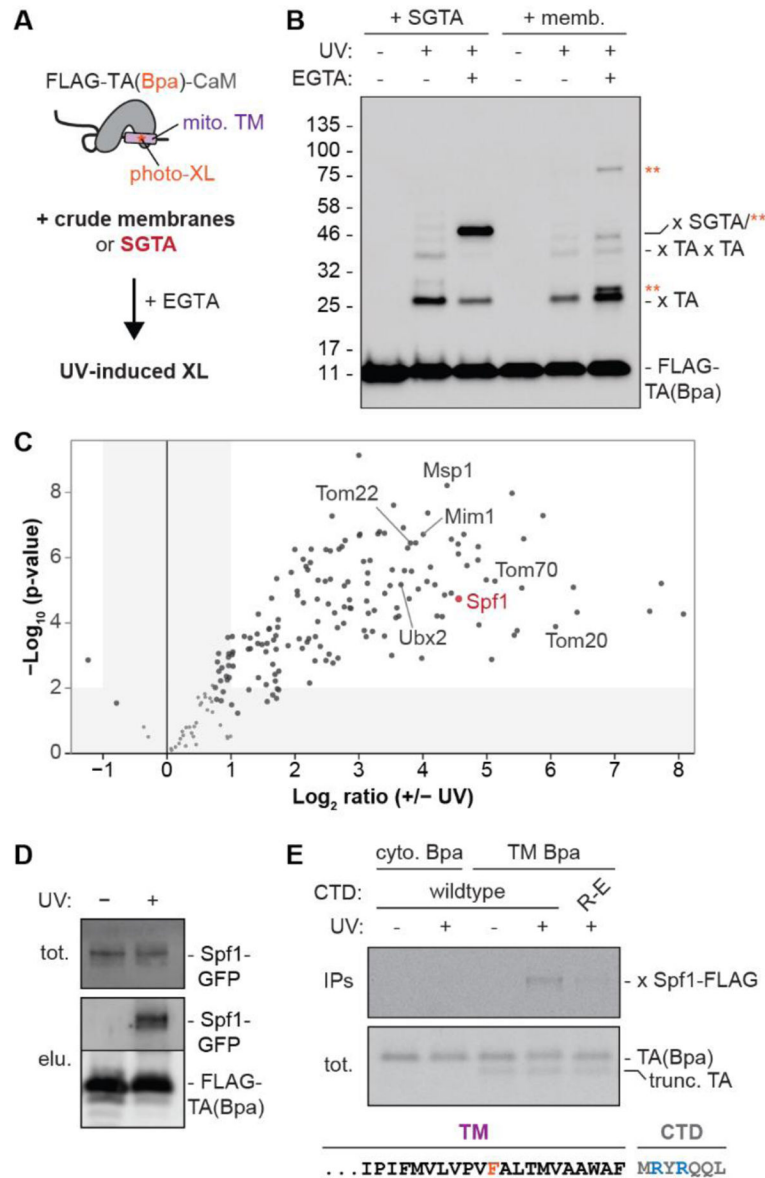
Fig. 1. The P5A-ATPase directly interacts with the TM of TA proteins.
(**A**) Scheme to identify direct interactors of a mitochondrial TA protein. Recombinant FLAG-tagged TA protein with the OMP25 transmembrane segment (TM) containing the UV-reactive crosslinker (photo-XL) Bpa was purified in complex with calmodulin [FLAG-TA(Bpa)-CaM]. EGTA dissociates FLAG-TA(Bpa) from CaM, permitting TM insertion into organelles in a crude membrane fraction or association with purified SGTA. Exposure to ultraviolet (UV) light induces site-specific covalent crosslinks. (**B**) Anti-FLAG blots of reactions as in (A). Unmodified FLAG-TA(Bpa) and FLAG-TA(Bpa) crosslinks of oligomers (x TA) and to SGTA (x SGTA) or membrane-specific proteins (orange asterisks) are indicated. (**C**) 6 replicates of reactions as in (A) without or with UV irradiation were affinity purified and analyzed by quantitative multiplexed mass spectrometry with tandem mass tagging (TMT-MS). Volcano plot shows relation of the P-value and $\log_2$ enrichment of

proteins by UV irradiation. (**D**) 5% input (tot.) of reactions as in (A) with organelles containing Spf1-GFP were purified via FLAG-TA(Bpa) (elu.) and immunoblotted for GFP to show UV-dependent Spf1 interaction. (**E**) Autoradiography of total (tot.) and denaturing anti-FLAG immunoprecipitations (IPs; top) of photocrosslinking reactions of in vitro translated radiolabeled untagged TA(Bpa) with organelles containing Spf1-FLAG. OMP25 TM and C-terminal domain (CTD) sequence is below. Bpa is positioned in the cytosolic (cyto.) domain (lanes 1-2) or the OMP25 TM (lanes 3-5). R-E, TA(Bpa) in which the arginines in the OMP25 CTD are mutated to glutamates; trunc. TA, truncated translation products that do not incorporate Bpa.
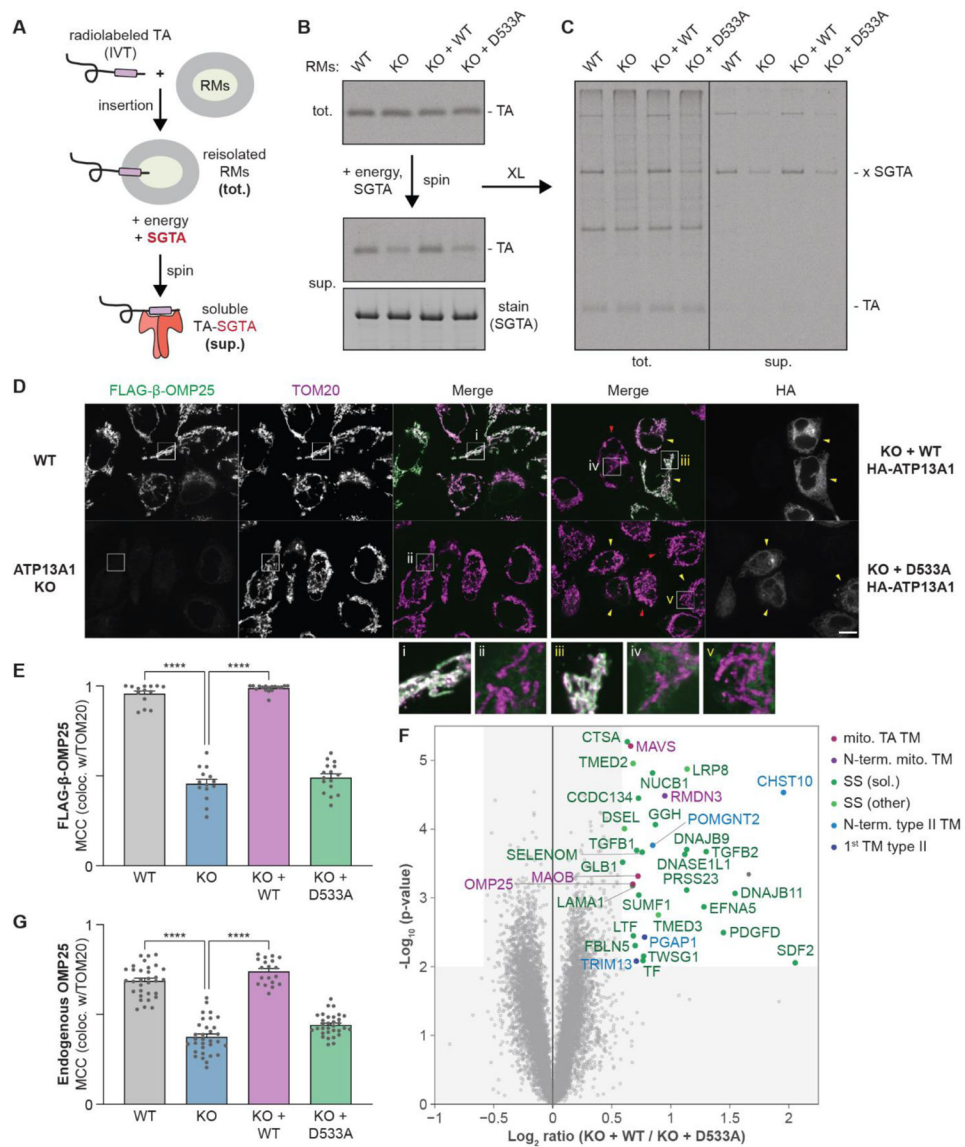
Fig. 2. ATP13A1 mediates TM removal from the ER.
(**A**) Scheme to reconstitute TA protein dislocation from ER-derived rough microsomes (RMs). In vitro translated (IVT) radiolabeled TA protein is incubated with RMs from wildtype (WT), ATP13A1 knockout (KO), or KO Flp-In T-REx 293 cells stably re-expressing wildtype (WT) or D533A ATP13A1. RMs containing inserted TA protein (tot.) are re-isolated and incubated with an energy regenerating system and the cytosolic TM chaperone SGTA. TA proteins dislocated from RMs are separated by centrifugation (sup.). (**B**) SDS-PAGE and autoradiography of tot. and extracted (sup.) TA protein containing the OMP25 TM with the indicated RMs. Equal recovery of SGTA (Coomassie) and TA protein crosslinks to SGTA (x SGTA) are indicated. (**C**) As in B, after crosslinking with 250 μM BMH. (**D**) Immunofluorescence of endogenous TOM20 (purple; mitochondrial marker) and FLAG-tagged TA protein containing the OMP25 TM (FLAG-β-OMP25; green) stably expressed in (left) WT, ATP13A1 KO, or (right) KO Flp-In T-REx HeLa cells transfected

with WT or D533A HA-tagged ATP13A1 (yellow arrowheads, transfected cells; red arrowheads, untransfected cells; also see fig. S5E). Scale bar, 10 μm. Panels below show high magnification views of boxed regions; intensity of FLAG-β-OMP25 is enhanced in ii, iv, and v. (**E**) Mean + s.e.m. and individual Manders' colocalization coefficient (MCC) values of FLAG-β-OMP25 colocalization with TOM20. **** $p<0.0001$. (**F**) Volcano plot showing relation of the P-value and $\log_2$ enrichment of proteins in ATP13A1 KO Flp-In T-REx HeLa cells re-expressing WT versus D533A FLAG-ATP13A1. Significantly enriched proteins are classified based on expected cellular localization and TM topology. mito., mitochondrial; N-term., N-terminal; SS, signal sequence; sol., soluble protein after SS cleavage. (**G**) Mean + s.e.m. and individual MCC of endogenous OMP25 colocalization with TOM20 in the indicated cells.
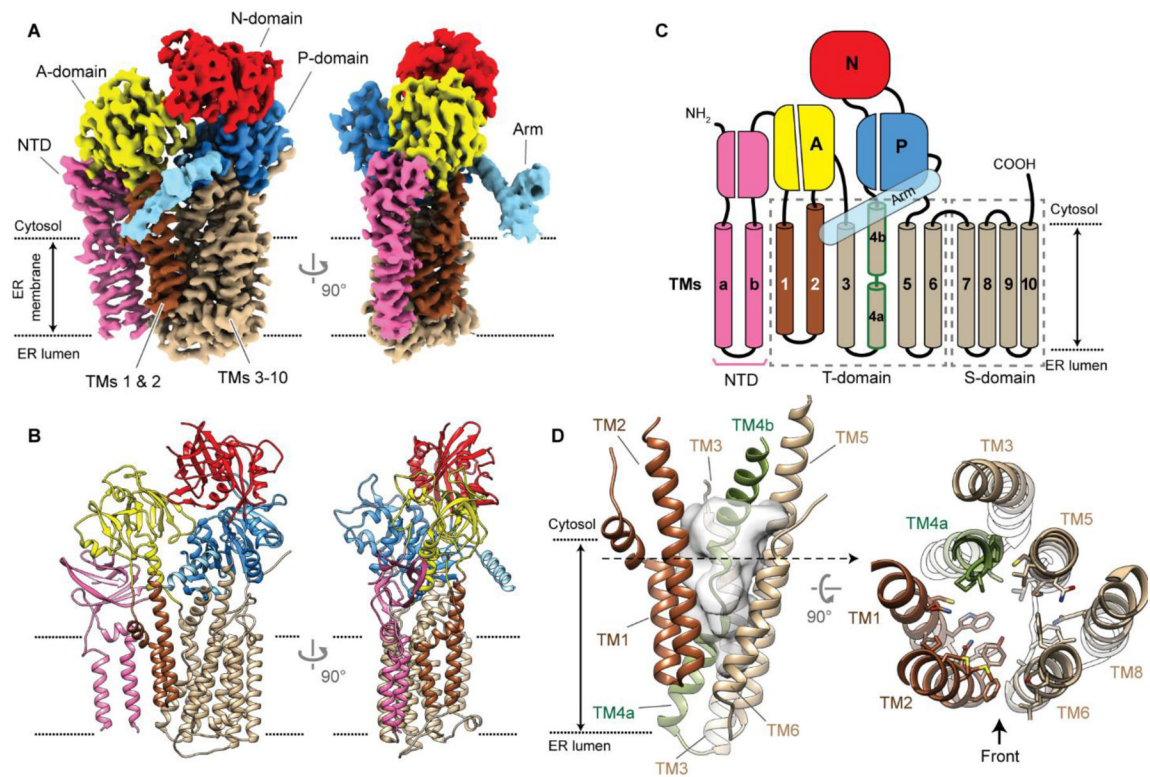
**Fig. 3. Structure of apo Spf1 in an inward-open conformation.**
(**A** and **B**) 3.5-Å-resolution cryo-EM reconstruction (A) and atomic model (B) of the apo Spf1. Note the 'V'-shaped opening of the substrate-binding pocket between TMs 1–2 (brown) and TMs 3–10 (tan). Dotted lines, the approximate boundaries of the ER membrane. (**C**) Domain architecture of Spf1. Note that the helix of TM4 (outlined in green) is unraveled halfway by a conserved PP(E/D)LP motif. (**D**) Views into the substrate binding pocket. Left, a front view. For clarity, only TMs 1–6 are shown. The solvent accessible volume (approx. 3,500 Å^3) is shown in semi-transparent gray. Right panel, a view from the cytosol (additionally, TM8 is shown). Side chains lining the cavity were shown in a stick representation.
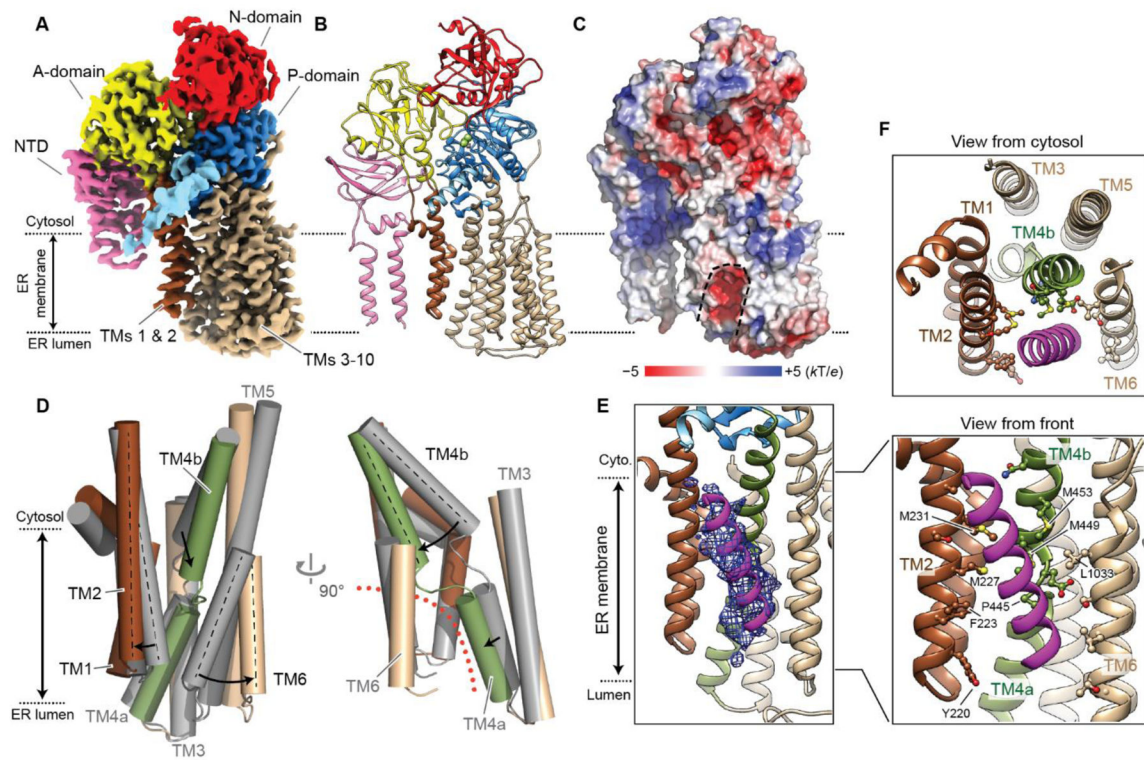
Fig. 4. Structure of Spf1 in an outward-open conformation.
(**A** and **B**) 3.3-Å-resolution cryo-EM reconstruction (A) and atomic model (B) of the BeF$_3$-bound Spf1. Shown are the front views. We note that unlike the inward-open structure, TMa and TMb are flexible in this conformation. TMa and TMb were modeled as polyalanine helices based on the apo structure. (**C**) A heatmap of surface electrostatics. Substrate-binding cavity is outlined with a dashed line. (**D**) Conformational changes of TMs 1–6 from the inward-open (apo; gray) to outward-open (BeF$_3$-bound; colored) states. Left, a front view; right, a side view. The outward-open substrate-binding pocket is indicated by an orange dotted line. (**E**) The density of copurified putative substrate (magenta mesh; 5-Å-lowpass-filtered) fitted with a poly-alanine helix model (also see fig. S20A). (**F**) As in E, but with amino-acid sidechains of Spf1 facing the substrate density shown in a ball-and-stick representation. Top, a cytosolic view; bottom, a front view.
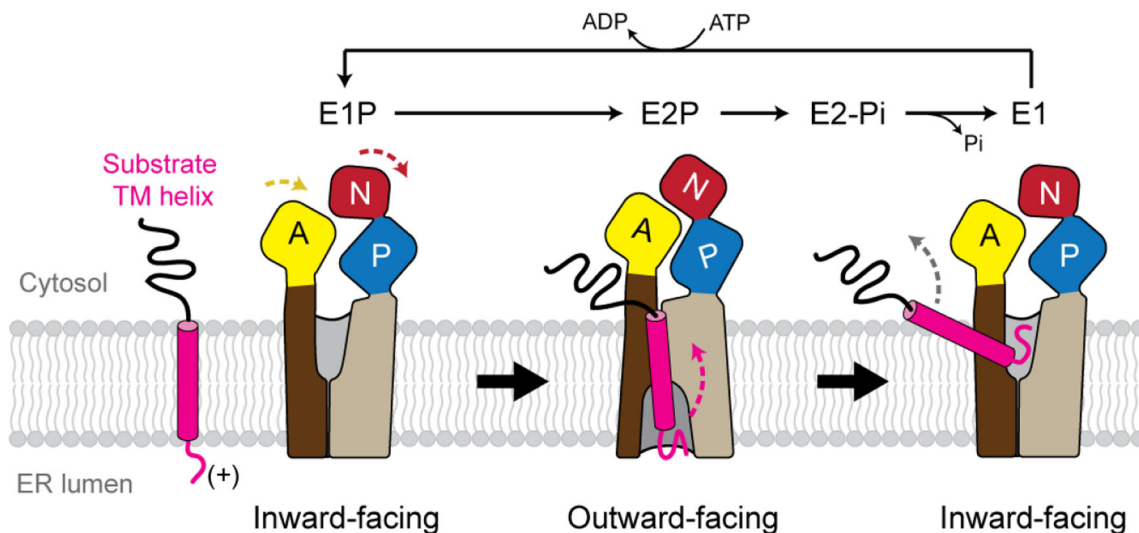
Fig. 5. Proposed model for TM dislocation by the P5A-ATPase.
The P5A-ATPase likely alternates between mainly two conformations, inward-open E1 and outward-open E2 states. During the E1P-to-E2P transition, the N domain rotates (red), and the A domain (yellow) moves closer to the N-P interface, causing conversion of the inward-open substrate-binding pocket of the transmembrane domain (brown and tan) to the outward-open conformation. In this model, a substrate TM helix (magenta) with a short, preferentially positively charged luminal segment would bind to the outward-open pocket and the E2P-to-E1 transition would flip the TM by a switch from the outward-open to inward-open conformation. For simplicity, some intermediate steps of the Post-Albers cycle are not shown.